The International Journal of Advanced Manufacturing Technology (2018) 96:2619–2642
https://doi.org/10.1007/s00170-018-1595-8

ORIGINAL ARTICLE

Numerical and experimental modeling of thermal errors in a five-axis CNC machining center

Marcelo O. dos Santos [1,2,3] · Gilmar F. Batalha [1] · Ed C. Bordinassi [2,3] · Gelson F. Miori [2]

Received: 8 September 2017 / Accepted: 9 January 2018 / Published online: 24 February 2018

Abstract

This work aims at the establishment of methodology to model and analyze the thermal errors of a five-axis CNC machining center, from an estimated temperature field, to finally model an artificial neural network (ANN) algorithm to accurately predict with robustness the thermal error. The thermoelastic behavior of the machining center was modeled through two different approaches: experimental (or data-driven) model and numerical (or physical) model. The thermal behavior of the machine was first modeled using finite element method (FEM) techniques based on theory of friction heat and convection heat and validated with the various experimentally raised temperature fields using temperature sensors and thermal imaging. The main machine subsystems were initially validated, such as ball screw system, linear guides, and spindle, which allowed for validating of the thermal behavior of the entire machine for five different duty cycles obtaining a maximum error of less than 8% when comparing the numerical results with the experimental results. The components of the thermal errors in *X*, *Y*, and *Z* directions were obtained through FEM by measuring the displacement of the spindle tip in relation to the reference bushing located on the worktable. The same procedure was experimentally performed using a touch probe system clamped in the spindle, and the results were compared obtaining a maximum deviation of 17 μm. The validation of the finite element model allowed for the use of the results obtained by the simulation to train and validate an ANN for predicting the thermal errors of the machining center. The relative errors between the thermal errors predicted by the ANN and the FEM simulation results were less than 1% indicating that the methodology developed in this work that combines the use of physical models with data-driven models is an accurate and robust tool to predict the thermal errors of the machine for various working conditions, even with the machine moving at different speeds or alternating the movement of the axles.

Keywords Thermal error · Finite element method · Machine tools · Precision · Accuracy · Robustness · Metrology · Artificial neural network

Nomenclature

T_b	Total friction torque in a ball bearing (N m)
T_{bl}	Friction torques due to the applied load in a ball bearing (N m)
T_{bv}	Friction torques due to the viscous effect in a ball bearing (N m)
H_{bf}	Total friction heat generated in a ball bearing (W)
T_n	Total friction torque of the ball screw nut (previous load and dynamic load) (N m)
H_n	Total friction heat generated by the ball screw nut (W)
F_{gf}	Frictional force in the linear guide (N)
H_{gf}	Total friction heat generated by the linear guide (W)

✉ Marcelo O. dos Santos
marcelo.santos@maua.br

Gilmar F. Batalha
gfbatalh@usp.br

Ed C. Bordinassi
ecb@maua.br

Gelson F. Miori
gelson@maua.br

[1] Department of Mechatronics and Mechanical Systems Engineering, Polytechnic School of Engineering of the University of Sao Paulo, Av. Prof. Mello Moraes, 2231, Cidade Universitária, Sao Paulo, SP 05508-900, Brazil

[2] Instituto Mauá de Tecnologia, Centro Universitário Mauá, Campus Sao Caetano do Sul – Praça Mauá 1, Sao Caetano do Sul, SP 09580 900, Brazil

[3] Mechanical Engineering Department, FEI—Centro Universitário da Fundação Educacional Padre Saboia de Medeiros, Av. Humberto de Alencar Castelo Branco, 3972, Bairro Assunçao, S. Bernardo do Campo, SP 09850-901, Brazil

P_h Magnetic power loss in the spindle motor (W)
P_{CU} Electrical power loss in the spindle motor (W)
P_f Mechanical power loss in the spindle motor (W)
H_m Total heat generated in the spindle motor (W)
h_1 Forced convection coefficient between ball screw shaft and ambient air (W/m^2 K)
V Slide unit speed for the three linear axes—$X/Y/Z$ (m/min)
L Machine stroke considered during the experimental tests (mm)

1 Introduction

The accuracy of machined parts, which is defined by the degree of conformity of the finished parts considering the geometric and dimensional specifications, is highly dependent on the performance of the machine tools. The accumulation and propagation of the errors through the kinematic structure of the machine tool is ultimately manifested directly in the dimensional variation of the machined parts [1]. Errors classified as quasi-static, such as geometric, kinematic, and thermal errors, are among the largest contributors of machine tool errors [2]. According to studies carried out by Bryan [3] and Aronson [4], thermal errors account for 40–70% of total machine tool errors. Therefore, the interaction between these errors must be modeled, controlled, and planned to ensure that the dimensions of the machined parts are in accordance with the increasingly demanding design specifications. Nowadays, machine tool manufacturers are continuously assuming the responsibility for the control of thermally induced displacements. This change occurred due to machine tool users realizing that machines which are similar in performance may present significantly different thermal errors [5]. According to [6], there are a lot of different approaches to model the thermoelastic behavior of machine tools in order to compensate occurring errors. Generally, these approaches can be divided in phenomenological models and physical models. Phenomenological models use empirically proven correlations between input parameters (e.g., temperatures) and an output value (e.g., tool center point (TCP) displacement). Experiments are carried out at different loads, and the results over time are approximated by a regression model (RM) or artificial neural networks (ANN) for example. Physical models as finite element method (FEM) models distinguish the calculation of thermally induced errors into the calculation of the temperature distribution using thermal load data and the calculation of the distortions in order to determine TCP deviations. This approach, based on the consideration of the underlying physical effects, enables an extrapolation so that any thermal load can be considered. At the same time, the separation into a calculation of the temperature field and a calculation of the distortions enables real-time applications [6]. In his research, Liu et al. [7] classified the thermal error modeling methods in data-driven model (DDM) and physically based model (PBM). The DDM model is based on the experimental data survey to represent the relation between the thermal error and the temperature of the machine tool, and then map thermal natural phenomena to mathematical equations while the PBM model allows to express the thermal behavior by explicit or implicit mathematical formula and does not need enough data to train models. According to Liu et al. [7], the advantage of PBM is that the model is designed based on heat transfer theory and geometrical structure, so the forecast bias will be small. Some techniques have been developed and implemented in machine tools to reduce the influence of thermal errors, including thermally symmetric machine design [8, 9], the introduction of additional cooling systems [10, 11], and thermal error compensation through measurements and simulation [12], as shown in Fig. 1.

In the last two decades, the International Organization for Standardization (ISO) published several standards such as ISO 230-3 [13], concerning temperature distortion of machine tools; ISO 10791-10 [14], concerning temperature distortion of machining centers; and ISO 13041-8 [15], concerning temperature distortion of turning machines. The thermal behavior of rotary axes is not included in any international standard yet and can only partly be derived from what has been specified in ISO 230-3 for linear axes, spindles, and the environmental temperature influence [6]. These standards provide methods for a systematic analysis of the thermal behavior of machine tools with main spindles. The present work includes the ETVE (environmental temperature variation error), as well as the thermal distortions caused by rotating (main) spindles and thermal distortions caused by moving linear axes. The measurement of the thermal distortion between the tool side and workpiece side is common in the standards, which usually uses a test mandrel clamped in the spindle and a setup with five displacement measurement devices fixed onto the table of machining centers [16]. According to Mayr et al. [16], using touch probes clamped in the machine tool spindle to detect the thermally induced TCP displacements has some advantages. With one probe, the thermally induced TCP displacements in up to three directions can be detected, and the thermal distortion can be detected at the center line of the machine tool spindle. Touch probes are often used to measure the displacements between machining operations. In such cases, the tool is replaced by a touch probe which detects the actual thermally induced TCP displacements, and a measurement setup with several detecting points is clamped at the table. The measurement procedure described in the standards is used for machine tools under no-load or finishing conditions [17].

Figure 2 shows two different procedures widely used to ensure thermal stabilization in the machining processes at industry. Figure 2a illustrates a touch probe for measuring the reference bushing located on the worktable, whereas Fig. 2b shows the temperature measurement of the workpiece by a probe clamped in the spindle. Both methods are used to

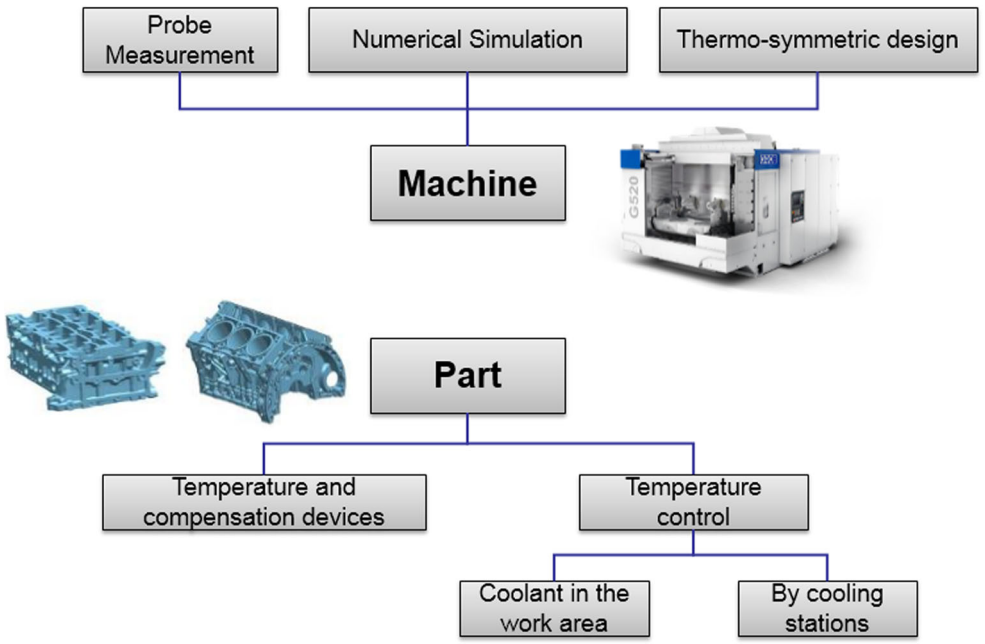

Fig. 1 Alternatives for thermal compensation in machine tool and in machined part

compensate the thermal error in real time, though penalizing the process with secondary time for both the measurement process and the tool change.

By analyzing the possibilities, it can be concluded that it may be more effective and profitable to compensate the thermal error by establishing an accuracy and robust mathematical model between thermal error and temperature. The thermal error can be predicted by measuring the temperature of the machine tool and compensating it in real time [18]. The accuracy and the robustness of the thermal error prediction model play an important role in the compensation effect using the method mentioned above. Robustness reflects the retention capability of predicted accuracy under varying external conditions, and it is a major indicator of the thermal error compensation effect of machine tools [19]. Generally, the strength of the correlation between the input variables of the model and the thermal error determines the accuracy of the prediction [20]. Since the temperature field of machine tools has nonlinear or temporal variability, its distribution is extremely complex. To obtain the temperature distribution, many temperature sensors are required, thus increasing the test costs and the workload of measurement and calculation errors. Simultaneously, the compensation model is affected by the multicollinearity between the temperatures read [21].

Several studies have focused on finite element method (FEM) and statistical methods to determine the appropriate modeling of the compensation algorithm to minimize the effect previously mentioned. Attia and Fraser [22] employed the FEM to analyze the overall temperature field of a CNC machine and divided the temperature field into a plurality of regular units according to the temperature field obtained in the simulation and the chosen correlation, thus determining the optimum number and the best position of the temperature measurement points. In [23], Xu et al. studied the influence of

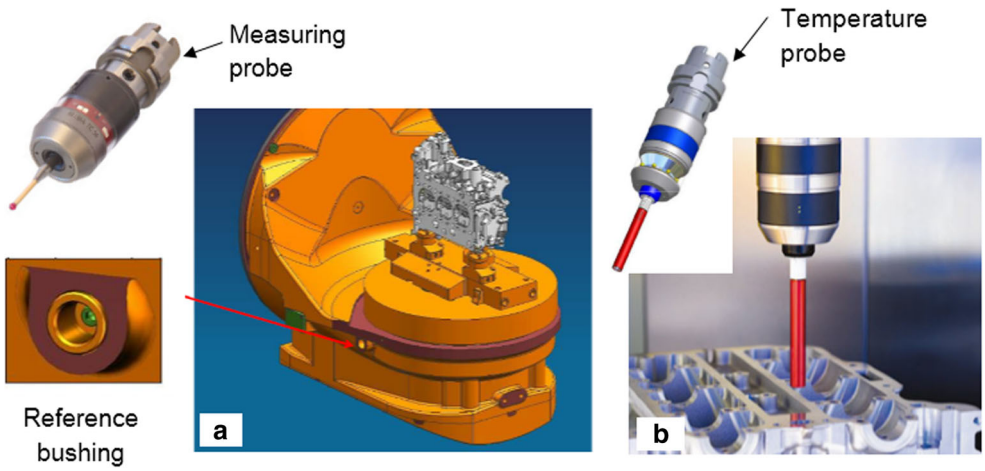

Fig. 2 Geometrical and thermal sensors. **a** Reference bushing and its measuring probe. **b** Temperature probe

temperature variation of the bearings in the transfer of heat of machine tools and improved the precision of the model of thermal error by FEM. In [24], Creighton et al. used the FEM to compensate the thermal error caused by the spindle of a high speed micro-milling machine tool. Although FEM has proven to be a good thermal error simulation feature in machine tool components, few studies have simulated the thermal behavior of the entire machine, mainly due to its complex modeling process [16].

Therefore, the statistical method is currently the most used to model the thermal error of machine tools due to its low cost and ease of use [25]. This method establishes an estimated thermal error when measuring actual thermal error and temperature of machine tools. Vanherck et al. [26] applied the ANN model to approximate complex multivariate nonlinear relationships and thus effectively compensated for the thermal deformation of multiaxis machine tools. Their results showed that the maximum deformation was reduced from 150 to 15 μm, and the machining error was reduced from 75 to 16 μm with the application of the neural model.

In [27], Yang et al. used the multivariate linear regression algorithm and neural network algorithm to establish the thermal error model and proved that both algorithms provided proper results. In [28], Mize and Ziegert used the neural network algorithm, based on diffuse artificial resonance theories, to establish a thermal error model to increase the robustness of the model against noise in the input variables. In [29], Zhang et al. established a thermal error model based on the combination of artificial neural networks and gray system theory, which can improve the learning efficiency and accuracy of the model. As studies highlighted show, statistical methods such as multiple linear regression, neural network, and support vector machine algorithms are still commonly used nowadays. The main idea behind modeling using these algorithms is to minimize the residuals of the model, thus guaranteeing robustness in predicting the estimated thermal errors [25].

Some gaps observed in the literature that served as motivation for the development of this research were

- Several works where the modeling and analysis of the thermal behavior of important subsystems of the machine tools were carried out in isolation, without correlating the combined effect of these components. As [30] that investigated the effect of thermal expansion on thermally induced errors of the ball screw system, such as [24, 31, 32] that analyzed and modeled the thermal behavior of the spindle, and as [33] that studied the effect of thermal error on machine tool slide guide motion. In the present work, all these subsystems were studied in an isolated way and later in a combined way to evaluate the thermal behavior of the entire machine tool.
- Studies based only on physical models such as [34], which modeled and simulated the thermal coupling for ball screw in boring-milling machining center, or studies based on experimental models such as [35, 36] that presented modeling methods and compensation of thermal errors based on data-driven acquisition. In the present work, a combined methodology of the two methods was developed.
- Few studies that studied the thermal behavior of a five-axis machine tool due to the complex influence of rotating axes on their kinematics.

Based on the research presented previously, this work, which is focused on the industrial application, intends to develop a combined methodology to study the thermal error of a five-axis machining center. The methodology will allow to use both the approach of phenomenological models with experimental data collection and the physical approach that considers the physical effects allowing an extrapolation of the thermal load. With this combined methodology of the two models, this work aims to increase the reliability of the predict model developed and allow a joint analysis of design and application engineering, to improve the thermal performance of the machine in future applications.

2 Materials and methods

2.1 Introduction to experimental procedure

Figure 3 shows the schematic of the complete work strategy of this research. However, this paper does not explore the implementation of the correction model in the CNC of the machining center. It is possible to observe in Fig. 3 that this work will use two different approaches to model the thermoelastic behavior of the machining center in order to show that contrary to what was presented in [6, 7], the phenomenological or data-driven model (DDM), and the physical or physically based model (PBM), can be complementary in order to achieve even more accurate and robust results.

The data-driven or experimental model was based on temperature and machine thermal error measurements for different duty cycles. The physical or simulation model was based on the modeling of the machine and its simulation through the FEM. All data experimentally collected were used to validate the finite element model of the machining center, as explained later in this research. The simulated data collected from the FEM analysis could be used to feed and train a neural network, thus allowing the developed algorithm to predict the behavior of the machine under untested working conditions.

Two main test stages were performed to survey the experimental data which served as reference for validating the FEM of the machine, classified as *preliminary validation stage* and *general validation stage*, respectively.

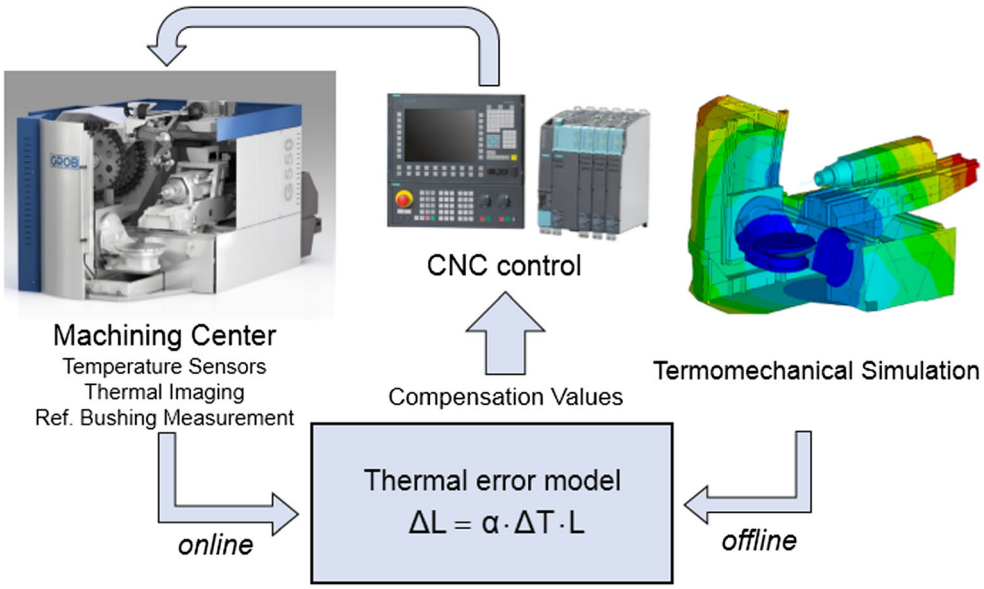

Fig. 3 Thermal error model research development strategy

In the preliminary validation stage, only two subsystems of the machine were evaluated, i.e., *X*-axis slide unit and (main) spindle. The movement cycle was defined with an *X*-axis speed of 30 m/min, and the spindle was set with rotation speed of 16,000 rpm in a 6-h cycle, with two more replicates being performed, totaling 18 h of tests. Only the temperatures of the ball screw nut and shaft, linear guide rail and carriage, and spindle tip were measured during this stage. This preliminary stage successfully permitted specifying and evaluating the thermal behavior of ball screw and linear guide systems of the *X*-axis, as well as the spindle of the machining center, which enabled the validation of the FEM of said subsystems. The success of the preliminary stage allowed the study of the entire machine, which occurred in the second stage. In the general validation stage, five different 4-h movement cycles were carried out in the machining center to evaluate the total thermal error, totaling 20 h of tests without replicates due to the long time span demanded. The slide units of *X*, *Y*, and *Z* axes were moved at two different speeds, simulating the usual working speeds of the machining center in industry, as indicated in Table 1.

The five cycles performed in this step were classified as cycles #1, #2, #3, #4, and #5, respectively. In cycle #1, only the *X*-axis was moving for a 4-h period with speed of $V_1 = 30$ m/min, in a stroke, $L_x = 800$ mm. In cycle #2, only the *Y*-axis was moving for a 4-h period with speed of $V_2 = 30$ m/min, in a total stroke $L_y = 950$ mm. In cycle #3, the *Z*-axis and the spindle were moving for 4 h with speed of $V_3 = 30$ m/min, in a total stroke $L_z = 600$ mm, and rotation speed of $n = 10{,}000$ rpm, respectively. In cycle #4, all three axes were simultaneously moving with speed of $V_4 = 30$ m/min and the spindle was moving with rotation speed of $n = 10{,}000$ rpm. Lastly, in cycle #5, the three axes were also moving; this time at the speed of $V_5 = 20$ m/min also with rotation speed of $n = 10{,}000$ rpm. A 14-h interval was taken between each cycle, by stopping the machine to return it to room temperature.

The machine studied is a GROB five-axis universal CNC machining center, which was installed in an environment with excellent ± 2 °C controlled ambient temperature (Fig. 4). The first goal in the experimental stage was to measure the complete temperature profile of the machine under different working conditions using temperature sensors and thermal imaging images. Simultaneously, the thermal errors in the *X*, *Y*, and *Z* axis directions of the machining center were measured using a touch probe. Thus, it was possible to evaluate the influence of the temperature in different points of the machine and their importance in the volumetric thermal error. In the next stage, a model of the machine was developed through the FEM approach with validation for all analyzes experimentally performed.

A total of 15 temperature sensors were installed in the machine and distributed at strategic points in the machine structure, aiming to accurately assess the thermal behavior of the machine in the different movement cycles. Figure 5

Table 1 *X*/*Y*/*Z* axis slide unit speed and ball screw rotation speed of the machining center

X/*Y*/*Z* axis speed (m/min)	*X*-axis ball screw rotation speed (rpm)	*Y*-axis ball screw rotation speed (rpm)	*Z*-axis ball screw rotation speed (rpm)
20.0	667	1000	800
30.0	1000	1500	1200

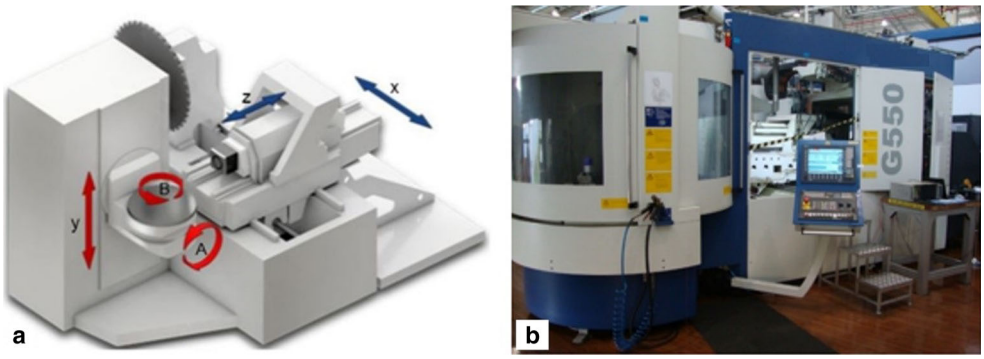

Fig. 4 The studied machining center. **a** Schematic representation of the five-axis kinematics. **b** The machining center

illustrates the exact placement of the 15 installation points of the sensors. Sensor T14 was submerged in the coolant tank of the machine to monitor the thermal behavior of the coolant passing through the base of the machine. The room temperature monitoring sensor T15 was installed outside the machine to avoid any influence.

Figure 6 shows photos of the temperature sensor T1 installed on the *X*-axis ball screw nut flange face (a) and the sensor T2 installed on the *X*-axis motor bearing flange face (b). An infrared camera was used to monitor the temperature at difficult access points, although it also monitored the flow of heat through the machine structure, thus confirming the data obtained from the thermal sensors.

An M&H touch probe type IRP40.1 was used to measure the displacement of the spindle tip in relation to the worktable. Figure 7a shows the procedure for measuring the thermal errors of the machining center, as well as the worktable and the measuring probe clamped in the spindle.

Figure 7b illustrates the reference bushing located on the side of the table and the probe tip close to the bushing, which measures its center coordinate. One of the strategies of this research was to evaluate the variation of the coordinates in the directions of the *X*, *Y*, and *Z* axes over time, as the temperature of the machine varies due to the friction generated in the movement of its slide components. The initial measurement is used as reference for the following thermal measurements, to reduce the influence of the machine geometrical errors.

2.2 Numerical simulation of the temperature field and thermal errors

Obtaining an analytical solution for the temperature field of the machining center has proved to be a challenging task, considering the transient heat flow in all directions and the various sources of heat such as motors, friction in the bearings, ball screws, and linear guides, as well as the heat exchange by natural and forced convection with the environment. Therefore, the FEM was used to obtain the numerical solutions for temperature fields and thermal errors of the entire machine. The numerical solution can be similar to the analytical solution, once the machine model is correct and has a suitable mesh and contacts, as verified by this research.

The reliability of the FEM simulation results also depends on whether the boundary conditions, such as heat generated and heat transfer coefficients, have been correctly defined. ANSYS Workbench (WB) and Classic ANSYS Parametric Design Language (APDL) were used to model and validate the thermal behavior and transient thermal errors of the

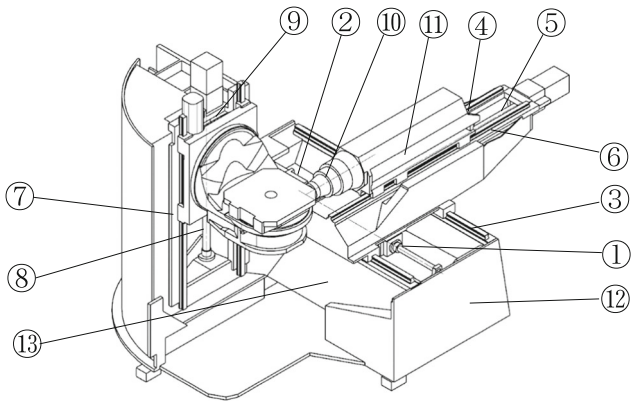

Fig. 5 Installation placement points of the 15 thermocouples in the machine tool

sensor	placement
T1	Ball screw nut (X-axis)
T2	Motor bearing flange (X-axis)
T3	Linear guide rail (X-axis)
T4	Ball screw nut (Z-axis)
T5	Motor bearing flange (Z-axis)
T6	Linear guide rail (Z-axis)
T7	Ball screw nut (Y-axis)
T8	Inside wall of column (Y-axis)
T9	Motor bearing flange (Y-axis)
T10	Spindle tip (Z-axis)
T11	Spindle housing (Z-axis)
T12	Machine base
T13	Working area
T14	Coolant tank
T15	Room temperature

machining center. Initially, the thermal behavior of two subsystems of the machining center was modeled and analyzed, i.e., *X*-axis slide unit (particularly simulating linear guides and ball screw systems) and spindle, in order to validate the FEM model by comparing the results of the data experimentally collected. After this validation, FEM analyses of the thermal errors for the entire machine were performed and compared with the errors experimentally measured during the five movement cycles of the machining center. For the purpose of this work, the use of FEM as an important method of modeling and predicting thermal errors was based on the following simplifying assumptions:

- Machining is not performed; thus, the chip effect is not considered.
- The grooves in the ball screw shaft were disregarded: hence, the ball screw shaft is a solid cylinder.
- The friction coefficient between the nut and the ball screw shaft surfaces, as well as between the bearings and the ball screw shaft, has constant value according to the manufacturer's specifications.
- The convective coefficients have constant values and were calculated according to the geometrical conditions of the machine components in addition to their movement situation.
- The effect of conduction of heat through lubricants and thermal deterioration was disregarded.

The general considerations for the FEM analyzes were as follows:

- Material of the machine base: steel St37-2-DIN 17100 (ISO 630-Fe360B)
- Ball screw shaft and linear guide rail material: steel AISI 52100-DIN 17230
- Slide unit housing material (*X*, *Y*, and *Z*): ductile cast iron GGG-60-DIN 1693-1/2
- Total analysis interval: 0 to 21,600 s
- The thermal mapping of the machine was considered every 360 s
- Thermal boundary conditions: based on the theory of heat convection and friction heat generated between the sliding elements of the machine

The heat generated by the friction was calculated for the subsystems that provided the highest heat rate for the machine, such as spindle, linear guide, and ball screw system and applied directed to the surfaces of the sliding elements. The forced convection coefficients for these components were also calculated. The analytical models used to calculate the thermal boundary conditions (TBC) are presented next.

2.2.1 Heat generation in bearings

The largest portion of the system heat generation is caused by the process of machining and friction between the balls and the bearing tracks [37]. However, in most cases, the machining heat is removed by the coolant and the chips; therefore, the friction between the balls and the bearing tracks is the predominant reason for raising the temperature of the system. According to Jafar [38], the total friction torque in a bearing is a measure of the energy loss in the contact surfaces of the bearing components, as well as the energy loss due to the viscous friction. The analytical estimate of the friction torque is overloaded with a multiplicity of factors, such as the friction between the rolling elements and the tracks and the cage, and the change in lubricant viscosity due to the increase in temperature, and therefore is accompanied by uncertainties [39].

An empirical relationship proposed by Palmgren [40] was used here, which was found to produce realistic results in notes of [41, 42]. Note that these formulas assume that there is an elastohydrodynamic film between the contact surfaces on the bearing side. The total friction torque in a ball bearing is given by Palmgren [40] using the relationship noted on [37, 41].

$$T_b = T_{bl} + T_{bv} \tag{1}$$

where T_{bl} and T_{bv} are, respectively, the friction torques due to the applied load and the viscous effect. The modified equation to consider the effect of the induced thermal preload [41] is as follows:

$$T_{bv} = 0,8 f_v (\mu_v n)^{2/3} (r_{in} + r_b)^3 \tag{2}$$

$$T_{bl} = \mu_l f_l (F_n + F_t)(r_{in} + r_b) \tag{3}$$

where f_v and f_l indicate the coefficient of rolling friction and the coefficient of sliding friction, respectively. F_n and F_t are the normal contact force and the thermally induced preload, respectively. The radius of the inner ring and the radius of the sphere are r_{in} and r_b, respectively, and μ_v is the viscosity of the lubricant. The speed rotation is indicated by n in rpm, and f_l is a coefficient related to the bearing direction, which depends on the bearing design as specified in the manufacturer's catalog. The total friction heat generated is given by

$$H_{bf} = \frac{2\pi n}{60} T_b \tag{4}$$

2.2.2 Heat generation on ball screw nut

According to Xu et al. [42], the principle of heat generation in the ball screw nut is very similar to that of ball

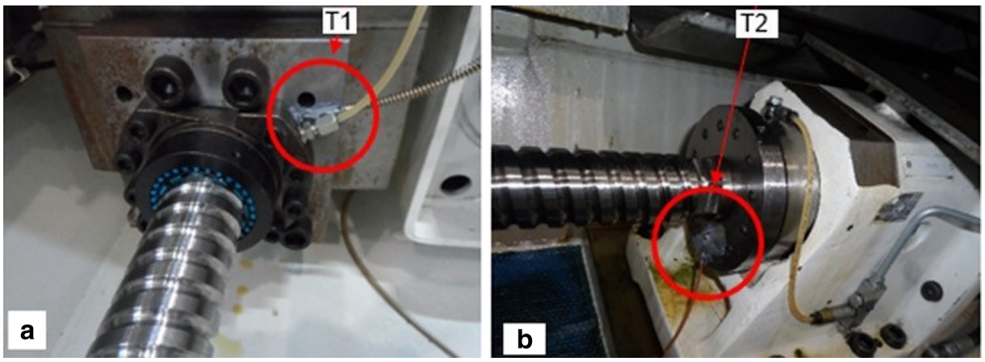

Fig. 6 Details of the thermocouple sensor placement on the machining center. **a** Thermocouple T1 installed on the *X*-axis ball screw nut flange face. **b** Thermocouple T2 installed on the *X*-axis motor bearing flange face

bearings in general. The heat is mainly generated by the friction between the balls and the grooves of the nut and between the balls and the grooves of the shaft of the ball screw. The nut load consists of two parts, i.e., the preload and the dynamic load. The total friction heat generated by the ball screw nut can be defined [43] as

$$H_n = 0,12\pi f_0 v_0 n T_n \tag{5}$$

where H_n is the total friction heat rate generated by the nut, f_0 is a factor related to the nut type and lubrication method, v_0 is the kinematic viscosity of the lubricant, n is the rotation speed of the ball screw, and T_n is the total friction torque of the nut (previous load and dynamic load).

2.2.3 Heat generation in the linear guide

In contrast to the heat generation model of bearings, which was developed by several researchers, the modeling of heat generation in linear guides has not been addressed [44]. The total frictional heat generated in a linear guide comes from the frictional force between the rolling elements, the rail, and the carriage. Almost all friction loss in a bearing is turned into heat inside the bearing itself, raising the bearing temperature. The total friction heat generated by the linear guide can be expressed as the heat rate (H_{gf}) under [45]

$$H_{gf} = \eta F_{gf} V \tag{6}$$

where F_{gf} is the friction force in the linear guide calculated from Eq. (7) and V is the speed. According to Cheng et al. [46], the friction force is a composition of the *Coulomb* friction force, the viscous friction, and the *Stribeck* effect force, which results in

$$F_{gf} = (0.315{-}0.03p_c)P \times 10^{-3} + \frac{1.52 p_c L_b}{v_i e^{-0.067(T-T_i)}} e^{-V/0.015} + L_b\left(0.003 L_b p_c V v_i e^{-0.067(T-T_i)} + 0.029\right) \tag{7}$$

where P is the external load, p_c is the preload class, and v is the kinematic viscosity. For the purpose of this study, the friction force was assumed to be completely converted into heat ($\eta = 1$) [45]. Subtracting Eq. (6) in

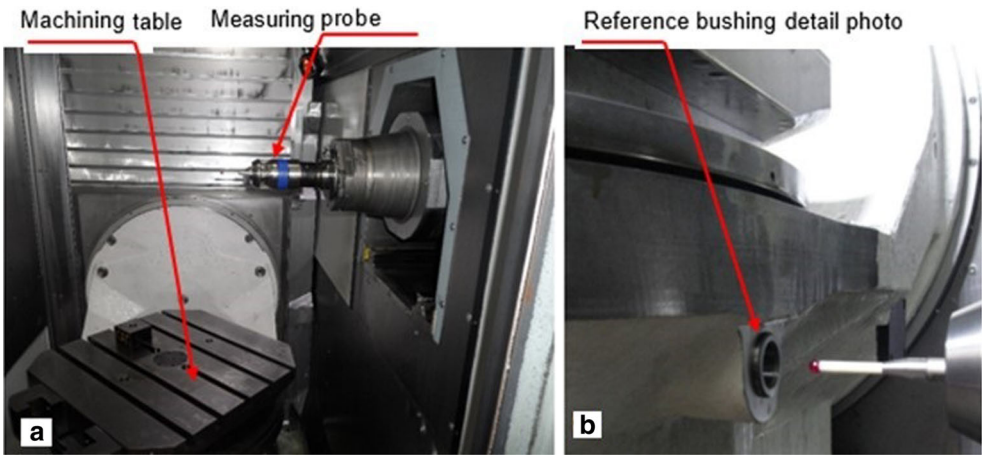

Fig. 7 **a** View of the machining center's working area. **b** Detail of the reference bushing on the worktable and the probe tip

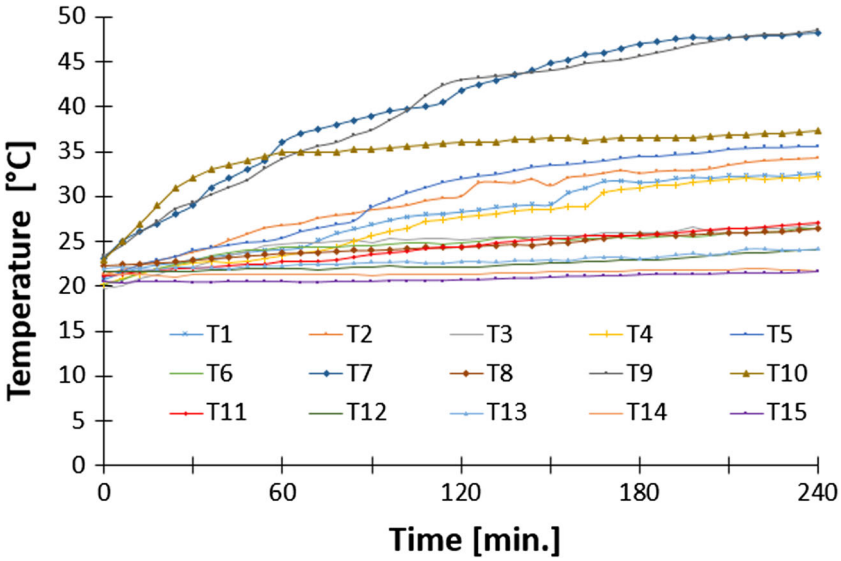

Fig. 8 Thermal behavior of the machine measured by the 15 sensors during cycle #4

Eq. (7) gives a relation for the generation of friction heat in the following way:

$$H_{gf} = (0.315{-}0.03p_c)VP \times 10^{-3} + V\frac{1.52p_cL_b}{v_ie^{-0.067(T-T_i)}}e^{-V/0.015} + VL_b\left(0.003L_bp_cVv_ie^{-0.067(T-T_i)} + 0.029\right) \quad (8)$$

This model facilitates obtaining various rates of friction heat by changing the operating parameters. The heat rate increases with increasing operating parameters such as speed (V), external load (P), and preload class (p_c).

2.2.4 Heat generation in the spindle

The models for the estimation of the thermal power of the bearings and the motor of the spindle are established as follows:

Bearings Generally, bearing heat is generated in the contact areas due to the friction between the balls and the internal and external tracks [37]. Thus, the thermal energy modeling H_{bf} (W) of the front and rear bearings of the spindle can be determined by Eq. (4) previously presented.

Motor The total heat generated H_m (W) in the motor is mainly attributed to its magnetic power loss P_h (W), electrical power loss P_{CU} (W), and mechanical power loss P_f (W), disregarding the additional loss [47]:

$$H_m = P_h + P_{CU} + P_f \quad (9)$$

In Eq. (10), the magnetic loss P_h (W) contains the loss of hysteresis P_t (W) and the current loss of eddy P (W), which can be calculated by

$$P_h = P_t + P_E \quad (10)$$

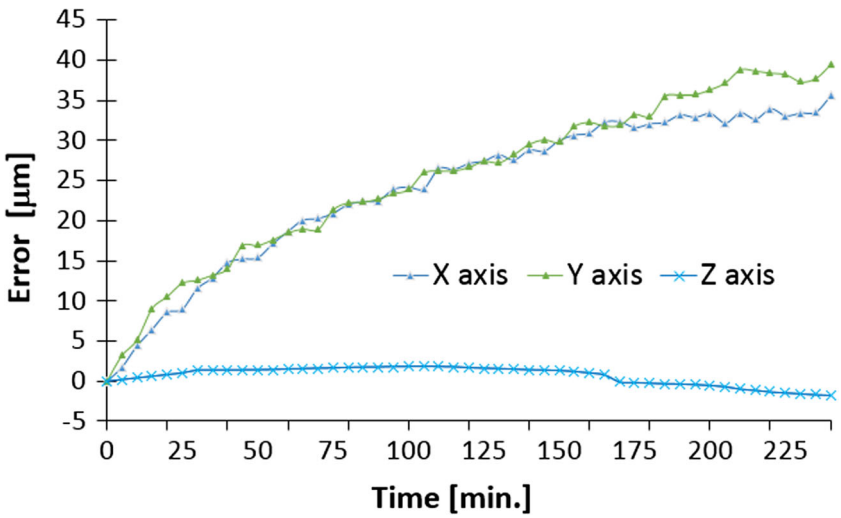

Fig. 9 Machine tool thermal error measurement during cycle #4

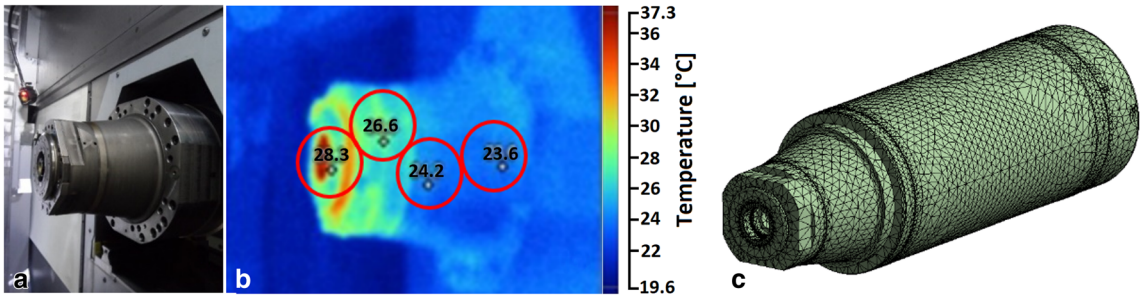

Fig. 10 Experimental and numerical analysis of the spindle **a** photo, **b** thermal image, and **c** spindle FEM meshing

being

$$P_t = CfB_{\max}^2 \tag{11}$$

$$P_E = \frac{\pi^2 t^2 (fB_{\max})^2}{6\rho\gamma_c} \tag{12}$$

In Eq. (11), C is a constant value related to the electric steel grades, f (s^{-1}) is the magnetization frequency, $B_{\max}$ (T) is the maximum magnetic flux density, t (m) is the thickness of the silicon steel sheet, and γ_c (kg/m^3) and ρ (Ωm) are the density and electrical resistivity of the iron core, respectively. Additionally, the electrical loss P_{CU} (W) in Eq. (13) can be calculated by

$$P_{CU} = \frac{I^2 \rho_C L}{S} \tag{13}$$

In Eq. (13), I (A) is the current and ρ_c (Ωm), L (m), and S (m^2) are, respectively, the resistivity, length, and section area of a conductor. Finally, the method for calculating of the mechanical loss P_f (W) in Eq. (14) is

$$P_f = \pi C' \rho_{ar} \omega^3 R_f^4 L_f \tag{14}$$

In Eq. (14), C' is the coefficient of friction, R_f (m) and L_f (m) are the outer radius and the length of the rotor, ϖ (rad/s) is the angular rotor velocity, and ρ_{ar} (kg/m^3) is the air density.

2.2.5 Coefficient of heat transfer by convection

The heat dissipation modeling of ball screw system, linear guide system, and spindle mainly includes natural convection heat transfer between their outer surface and the air, as well as forced convection heat transfer between the movable parts and the circulating air. A literature review on the convection coefficient formulations used in this research is presented next.

Forced convection between ball screw shaft and ambient air

Heat transfer by forced convection between the nut and the shaft and forced convection of the shaft with the cooling fluid was considered in [48]. During the work cycle of the machining center, the ball screw spins at a certain speed, which will accelerate the convection with the air. This is known as the forced convection and the

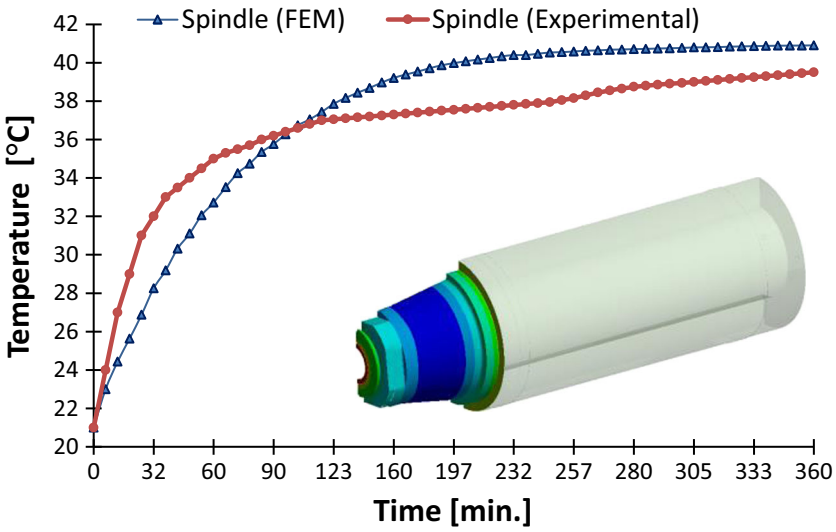

Fig. 11 Comparison of the thermal behavior of the spindle: experimental sensor reading T10 versus temperature predicted by FEM analysis

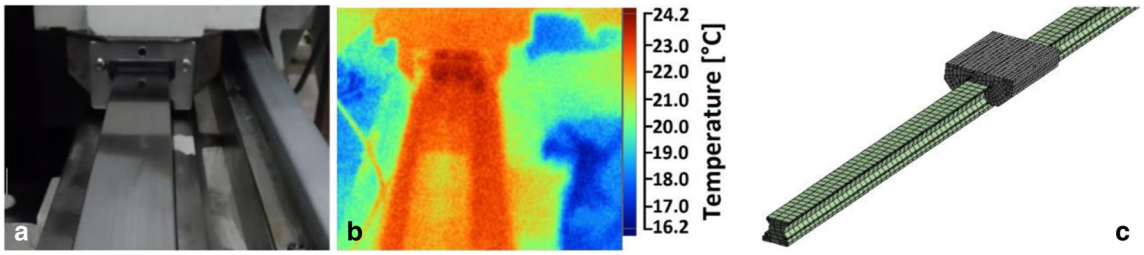

Fig. 12 Experimental and numerical analysis of the *X*-axis linear guide **a** photo, **b** thermal image, and **c** finite element meshing

heat transfer coefficient (W/m^2 K) by convection, defined [49] as

$$h = N_u k_{fluid}/d \tag{15}$$

being N_u the Nusselt number, which is calculated from the Reynolds number R_e and the Prandtl P_r number as shown in Eq. (15), k_{fluid} is the thermal conductivity of ambient air, and "d" is the outside shaft diameter (mm) when convection occurs on the outer surface of the cylinder, as seen in this work.

$$N_u = 0.133\mathrm{Re}^{2/3}\mathrm{Pr}^{1/3} \tag{16}$$

where

$$\mathrm{Re} = u_{fluid}d/v_{fluid} \tag{17}$$

$$\mathrm{Pr} = c_{fluid}\mu_{fluid}/k_{fluid} \tag{18}$$

In Eq. (17), u_{fluid} is the air flow velocity and v_{fluid} is the kinematic viscosity of the air. In Eq. (18), c_{fluid} is the specific heat capacitance of air and μ_{fluid} is the dynamic viscosity of the air. Thus, the convective coefficient of the external surface of the ball screw shaft "h_1" in Eq. (19) in [44] can be easily found.

$$h_1 = 0,133 \times \left(\frac{u_1 d_1}{v_{fluid}}\right)^{2/3} \times \left(c_{fluid}\mu_{fluid}/k_{fluid}\right)^{1/3} \times k_{fluid} \tag{19}$$

where u_1 is the relative velocity on the outer surface of the ball screw shaft and d_1 is the external diameter of the shaft.

Forced convection between the spindle and the ambient air

When the spindle rotates, air circulates around its surfaces at a constant velocity, which according to [50] can be modeled as air along a flat plate characterizing convection forced by

$$h_4 = 0.664\frac{k}{l}\mathrm{Re}^{1/2}\mathrm{Pr}^{1/3} \tag{20}$$

where

$$\mathrm{Re} = \frac{u_2 l}{v}; \tag{21}$$

$$u = \frac{\pi d_2 n}{60}; \tag{22}$$

$$l = \pi d_2 \tag{23}$$

where u_2 is the relative velocity on the outer surface of the spindle and d_2 is the external diameter of the spindle.

3 Results and discussion

This paper presents the experimental data from representative cycle #4 only, since there are several batches of experiments which could not provide all the experimental data. The

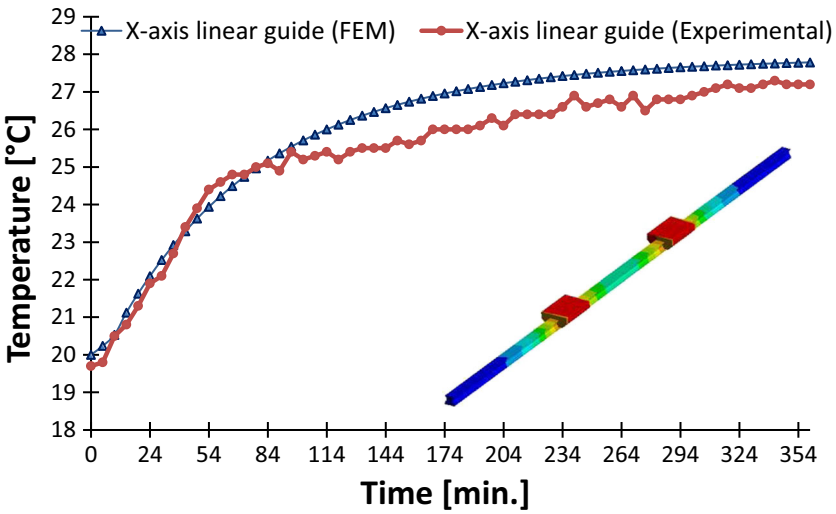

Fig. 13 Comparison of the thermal behavior of the linear guide: experimental sensor reading T13 versus temperature predicted by FEM analysis

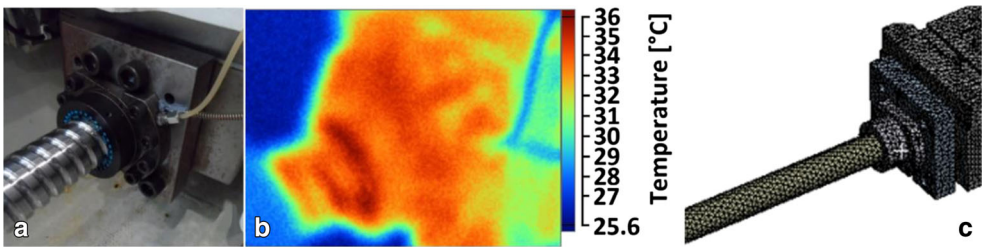

Fig. 14 Experimental and numerical analysis of the *X*-axis nut **a** real image, **b** thermal image, and **c** finite element mesh (FEM)

temperature curves experimentally read by the 15 sensors are shown in Fig. 8. The thermal stabilization of the spindle could be observed after approximately 60 min, while the ball screw nut and the motor bearing flange of *Y*-axis reached the highest temperatures and stabilized only after approximately 4 h.

Figure 8 demonstrates also that the temperatures read by the sensors T7 and T9 located in the ball screw nut and in the bearing motor flange of the *Y*-axis showed the highest increase, particularly in this machine movement cycle in which the three linear axes were driven. Subsequently, there was an increase in the temperature of the spindle tip, which had a faster stabilization, and in the temperature of the ball screw motor bearing of *X* and *Z* axes, respectively. Similarly, the ball screw nuts of *X* and *Z* axes showed high temperatures, displaying a comparable behavior. The temperatures T11, T12, and T13, which represent the temperatures read on the spindle housing, machine base, and working area, respectively, showed small variations caused by the heat generation in the servo-motors, as well as the heat friction of the components in their related motion. Finally, the temperature of the coolant and the ambient temperature did not undergo significant changes, as expected.

Figure 9 shows the experimental thermal error in the *X*/*Y*/*Z* axis direction obtained during cycle #4. Observed in Fig. 9 is that the values of thermal error measured during cycle #4 in the *X* and *Y* directions are similar, however having slightly different values, indicating the increase in error coinciding with the increase in temperature of the respective slide units. The error in the *Z* direction indicates an approximation of the spindle tip in relation to the worktable, which was expected by analyzing the assembling conditions. The other experimental results of the thermal errors obtained during cycles #1, #2, #3, and #5 will be shown in comparison with the results from the FEM simulation later in this paper.

3.1 Numerical simulation of machine subsystems

The thermal simulations were carried out in the machining center's *X*-axis slide unit comprising the ball screw and linear guide systems, in addition to the spindle. The FEM results were constantly compared with the experimental results in order to validate the transient thermal behavior simulated at ANSYS. The thermal loads and the heat transfer coefficients by convection were calculated using the equations previously mentioned for all the analyzed cases. This step aimed to evaluate the use of numerical modeling using the thermal boundary conditions based on the theory of frictional heat and heat convection.

3.1.1 Spindle transient thermal analysis

The heat generated in the rear bearing equaled 147 W; the heat generated in the front bearing equaled 93 W, and the heat generated in the motor equaled 342 W, with a spindle speed of

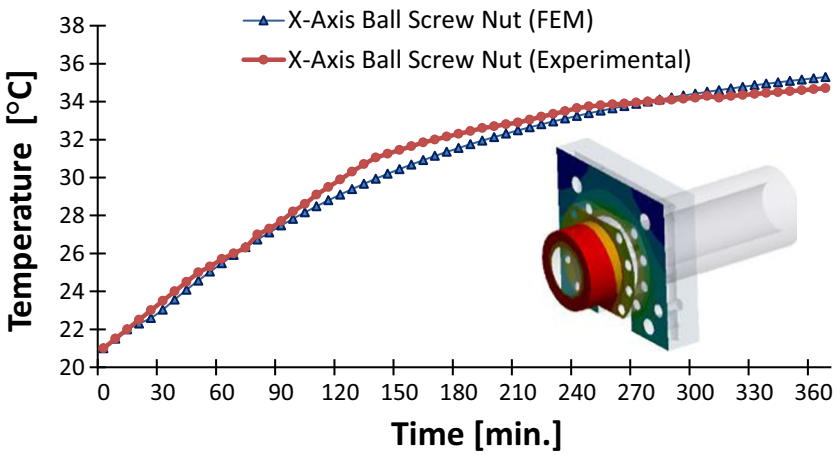

Fig. 15 Comparison of the thermal behavior of the ball screw nut: experimental sensor reading T1 versus FEM temperatures predicted by simulation

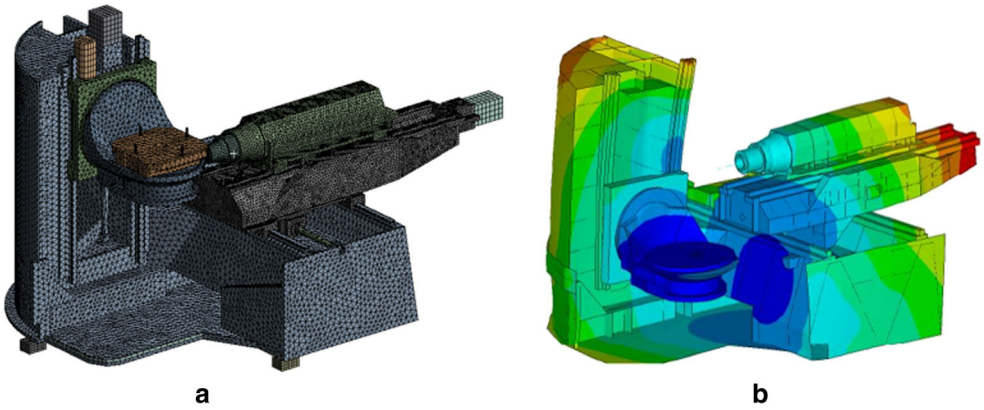

Fig. 16 Machining center FEM analyze **a** finite element mesh and **b** temperature field

16,000 rpm, considering the surrounding air. The front bearing displayed a restriction to the axial displacement to decrease the effect of the spindle tip expansion, whereas the rear bearing moved freely in the axial direction. The forced convection heat transfer coefficient on the outer surface of the calculated spindle tip was 58 W/m^2 K. Figure 10 shows the photo of the spindle tip in the machining center (a), its thermal image (b), and the finite element meshing (c). A 10-node tetrahedral mesh with 20-mm element was used.

Figure 11 shows the graph of the comparative evolution of the thermal behavior during the experimental measurements and the numerical analysis during a 6-h operation with a 16,000 rpm speed. Note that the experimentally measured temperature increased quicker than the temperature obtained through the simulation. This is due to the need to adjust the forced convection thermal boundary condition at spindle tip. However, observe that both temperatures reached virtually the same final temperature. The final temperature obtained in the spindle tip region by FEM was 40.89 °C, whereas the temperature obtained experimentally was 39.40 °C with a relative error of 3.8%. The largest errors occurred at the beginning of the analysis since the thermal stabilization in the simulation occurred more slowly. In the first 30 min, the maximum error reached 8.6%.

3.1.2 *X*-axis linear guide rail transient thermal analysis

At an *X*-axis slide unit speed of 30 m/min, the heat rate at the contact between the carriage and the rail reached 18 W, with a friction coefficient, $\mu = 0.35$. The convective heat transfer coefficient at the rail surface was 20 W/m^2 K. Figure 12 shows the image of the *X*-axis linear guide (the rail and carriage) (a), a thermographic image (b), and the FEM meshing (c). The type of element used was the 20-node hexahedron with element size of 20 mm in the guide and 10 mm in the carriage.

Figure 13 graph demonstrates the measurement and simulation results at one measurement point on the rail for the first 6 h of rail heating due to operation. The carriage moved back and forth at a constant velocity of 30 m/min. Between the end points of an 800-mm stroke, model adjustment, particularly quantification of the boundary conditions, such as moving friction and thermal conduction to the coupling structures, was conducted through experimental measurement values for heat build-up over the longer term. The temperature curves as a

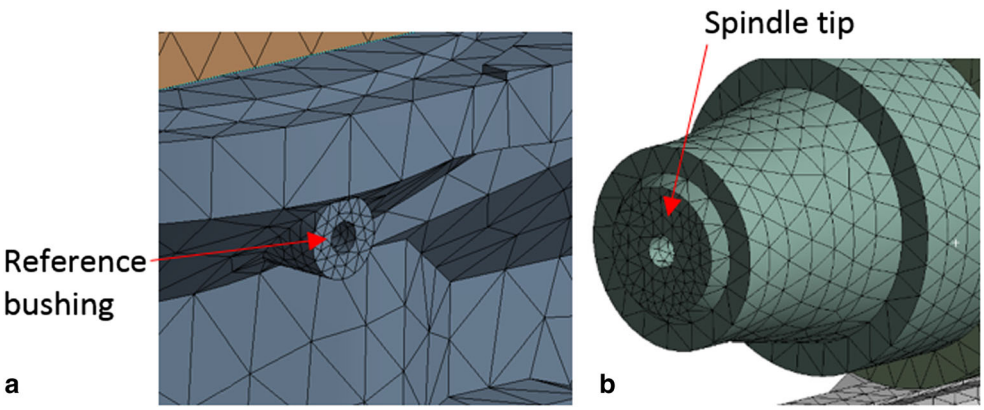

Fig. 17 FEM refined mesh regions. **a** Reference bushing on the table. **b** Spindle tip

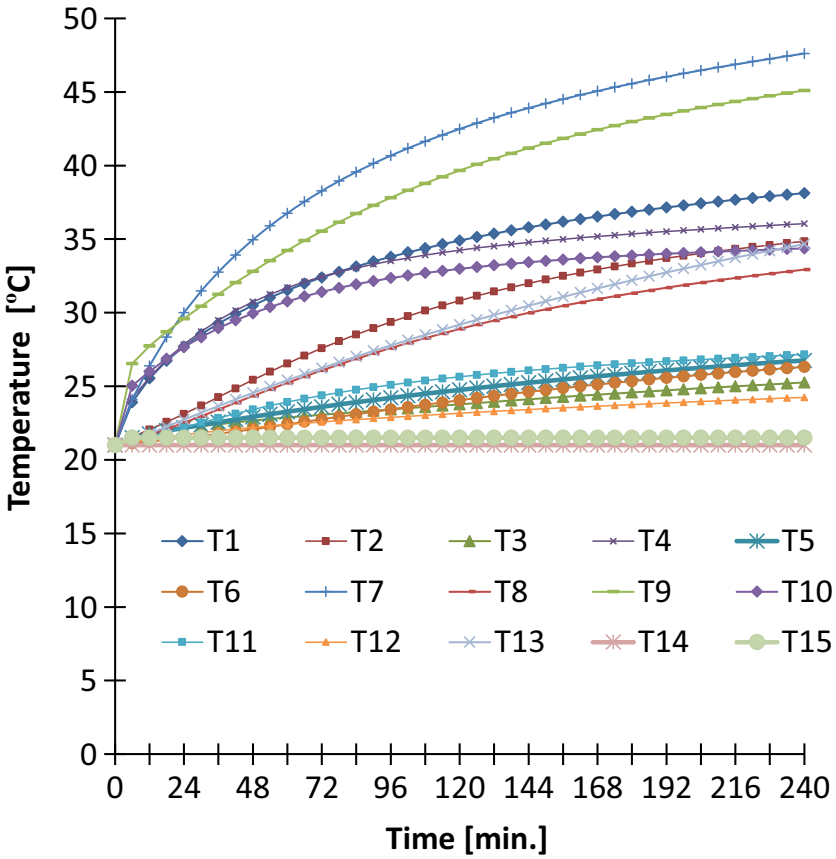

Fig. 18 Temperature curves for all thermocouple measuring points during cycle #4

function of time (see Fig. 13) confirmed that the model had accurately mapped the heat buildup on the rail. The final temperature obtained in the linear guide trail by FEM was 27.79 °C, whereas the temperature experimentally obtained was 27.20 °C with an error of 2.1%.

3.1.3 *X*-axis ball screw nut transient thermal analysis

At an *X*-axis slide unit speed of 30 m/min, the heat generated at the contact of the nut with the shaft reached 48 W with friction coefficient equaled to 0.38.

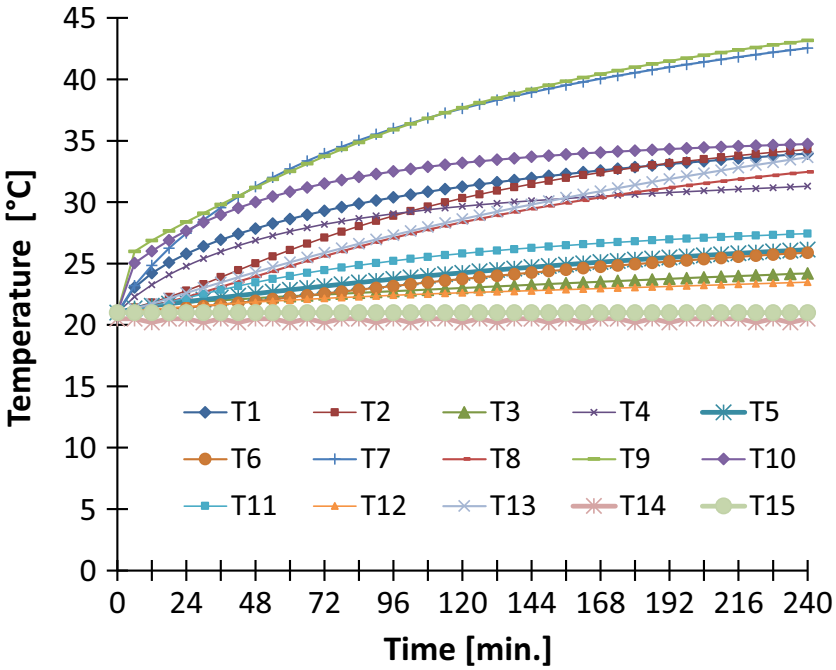

Fig. 19 Temperature curves for all thermocouple measuring points during cycle #5

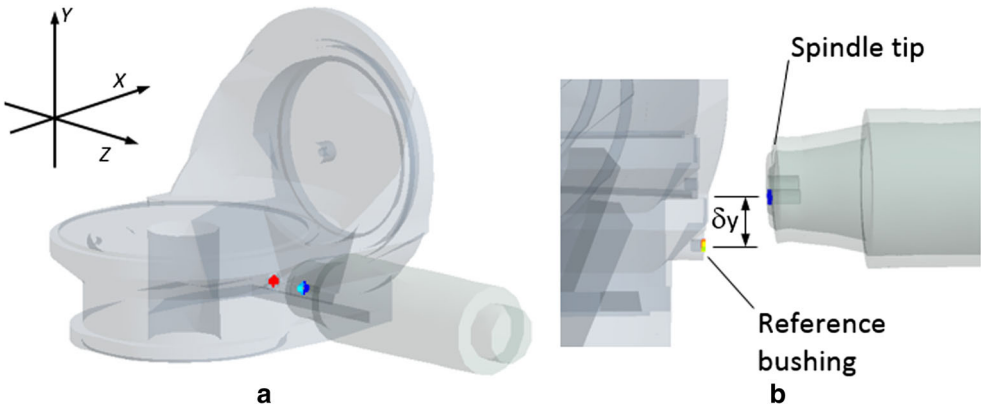

Fig. 20 Simulation of the machining center thermal error. **a** Perspective view with indication of the reference system. **b** Large-scale detail of thermal error measured in *Y*

The heat rate in the front bearing reached 12 W, while the heat rate in the rear bearing reached 17 W. The convective heat transfer coefficient between the shaft surface and the ambient was 42 W/m^2 K, and at the nut surface was 34 W/m^2 K. Figure 14 shows the ball screw nut photo (a), a thermal image (b), and the corresponding finite element meshing (c), composed of a 10-node tetrahedral element type, a 10-mm element in the shaft, and 15 mm in the nut.

Figure 15 illustrates the comparative evolution of the thermal behavior during the experimental measurements with the numerical analysis during a 6-h operation with 30 m/min speed. Note that the ball screw nut temperature rose as a function of time and that the value obtained with the simulation precisely coincides with the value experimentally obtained (see Fig. 15). This increase in temperature was due to the heat generated by the friction between the nut and the ball screw shaft contact in the round-trip displacement through an 800-mm course. The final temperature obtained in the linear guide trail by FEM was 35.30 °C, whereas the temperature experimentally obtained was of 34.70 °C, with an error of 1.7%.

3.2 Numerical simulation of the entire machine

After validating the temperature fields for the *X*-axis ball screw, linear guide, and spindle, the thermal boundary conditions, as well as the friction contacts created in the previous simulation, were used as initial boundary conditions in the transient thermostructural analysis of the entire machining center for all five experimental cycles performed. In the FEM machine model, 409,786 second-order tetrahedral elements were used, totaling 737,629 nodes with element size of 50 mm in the machine structure, 40 mm in the worktable, and 25 mm in the slide units (see Fig. 16). The 10-node tetrahedral elements of 10 mm were used around the reference

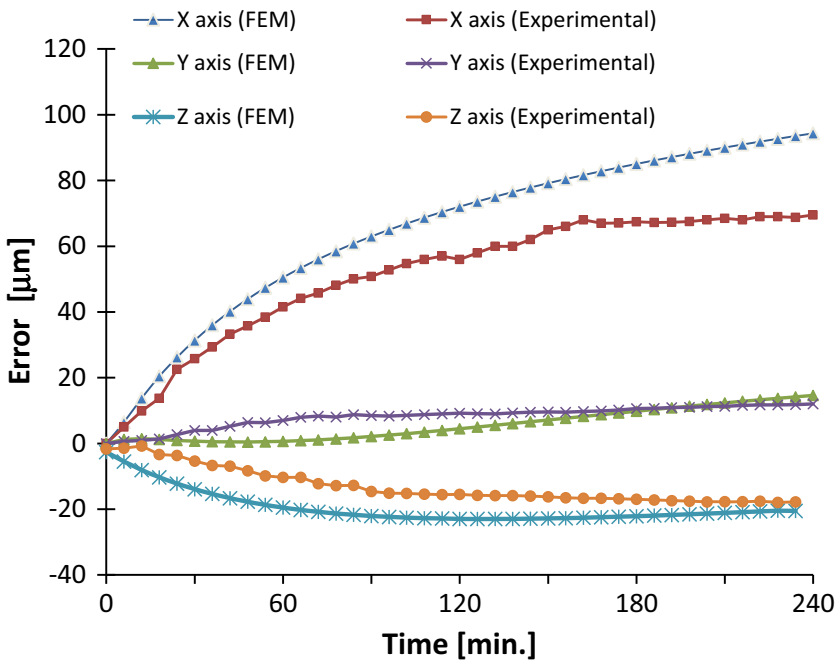

Fig. 21 Thermal errors obtained by experimental tests and FEM during cycle #1

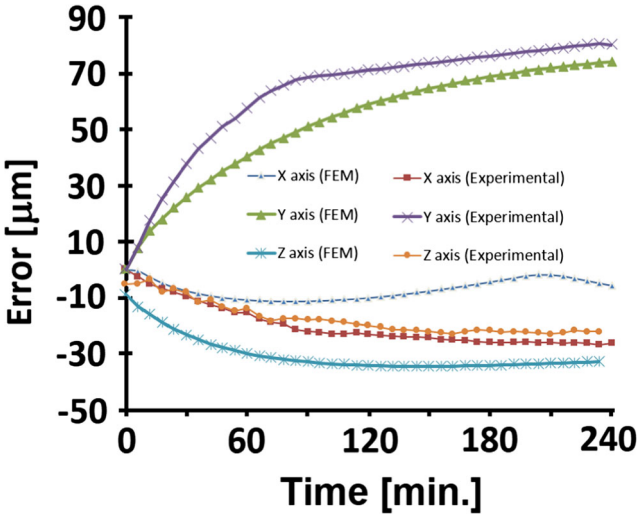

Fig. 22 Thermal errors obtained by experimental tests and FEM during cycle #2

bushing hole (see Fig. 17a), and in the spindle tip region (see Fig. 17b), to ensure more accurate results.

3.2.1 Analysis of temperature field: FEM simulation results

As presented in item 2.1, the five test cycles performed in the machining center were numerically simulated by FEM. Only the graphs of the temperature field obtained by the simulation of cycle #4 (see Fig. 18) and cycle #5 (see Fig. 19) are presented due to the large number of results collected. The comparison of the simulated temperature field for cycle #4 results (see Fig. 18) with the experimental results illustrated in Fig. 8 demonstrates the same lines of thermal behavior. Moreover, observe that the T7 and T9 sensors showed the highest increase in temperature among the other readings. The maximum relative error was 4.65% for the temperature of the *Y*-axis ball screw nut, which is due to the difficulty of accurately simulating the convective heat transfer inside the machine column ambient.

Observe in Fig. 19 that the heating tendency of the 15 points analyzed in the machine for cycle #5 was the same as seen in cycle #4 (see in Fig. 18). However, due to higher slide axis speeds in cycle #4, the temperatures were higher at the points exposed to friction heating. The room temperature as well as the coolant temperature and the machine base temperatures remained virtually unchanged during cycles. Note that the spindle tip temperature indicated by virtual sensor T10 remains practically unchanged, due to the spindle speed during cycle #5 being the same as in cycle #4, i.e., n = 10,000 rpm.

The experimental and simulation results of the temperature fields of the machining center subsystems seen in Figs. 11, 13, and 15 were obtained during the preliminary validation stage. These results confirmed the accuracy of the simulation model adopted, which allowed to replicate the thermal boundary conditions to simulate the thermal behavior of the entire machine for cycles #1, #2, and #3, not shown in this paper, and cycles #4 and #5 (see Figs. 18 and 19) obtained during the general validation stage, thus allowing a robust FEM simulation of the thermal errors of the machine for each of the conditions experimentally analyzed. The results of simulated thermal errors for each of the cycles performed are presented next in comparison with the experimental results.

3.2.2 Analysis of thermal error simulation results

During FEM numerical simulations, the thermal errors were obtained by measuring the relative error between the spindle

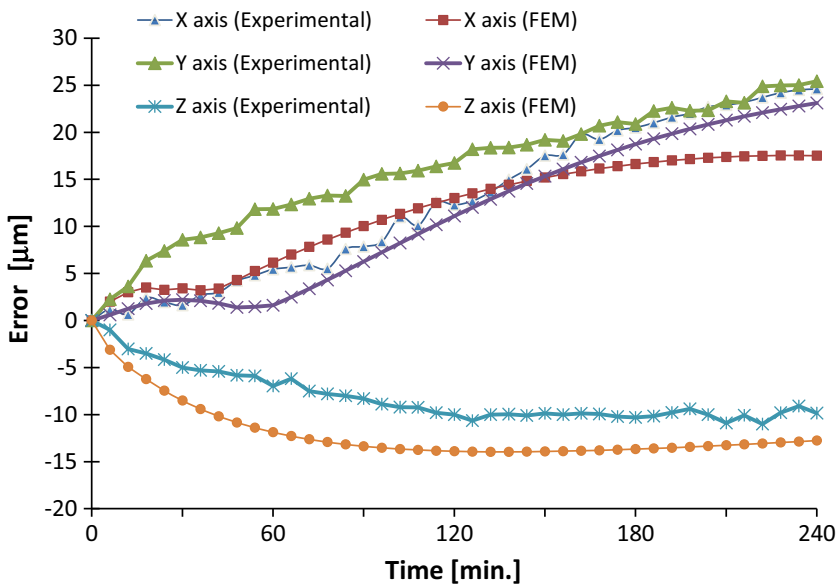

Fig. 23 Thermal errors obtained by experimental tests and FEM during cycle #5

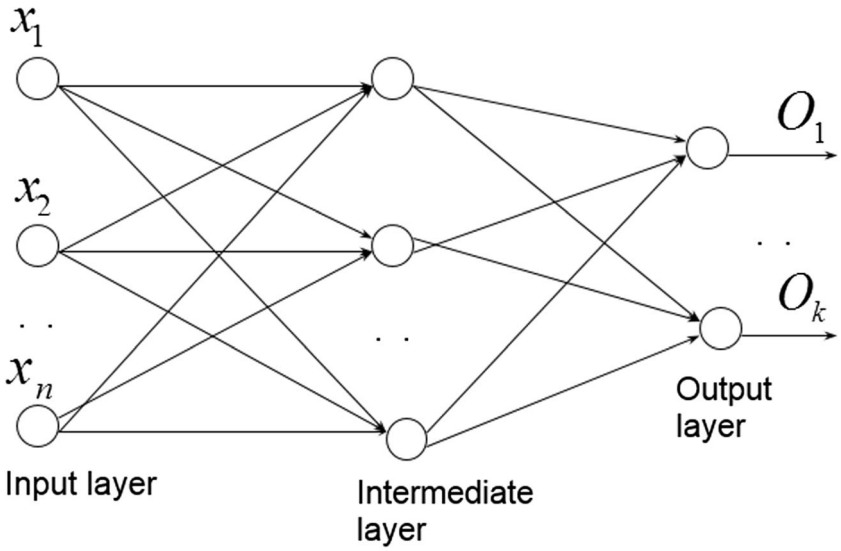

Fig. 24 Neural network model structure

tip and the reference bushing located on the worktable, thus replicating the measurement of the thermal errors during the experimental steps (see in Fig. 8). Figure 20 shows the perspective view of the worktable and spindle isolated from the rest of the machine, i.e., (a) a close view in detail of the thermal error obtained in the *Y* direction and (b) and in large scale for the purpose of better understanding the measurement strategy.

The thermal errors in the *X*, *Y*, and *Z* axis directions were obtained by FEM for the cycles #1, #2, #3, #4, and #5 using the methodology previously described. Only the results of the thermal errors in cycles #1 (Fig. 21), cycle #2 (Fig. 22), and cycle #5 (Fig. 23) are presented and consequently discussed in this paper due to the large number of results collected. All the corresponding thermal error curves experimentally obtained were also added to the graphs to show the accuracy and robustness of the FEM analysis when simulating the thermal error of the machining center.

Figure 21 shows the experimental and simulated results for cycle #1, in which only the *X*-axis was moving in the machine, while the other two linear axes were in idle mode. Observe that for Fig. 21 results, in both cases, the thermal error in the *X*-axis direction was higher and continuously increasing, i.e., the distance between the reference bushing and the spindle tip in the *X*-axis direction increases. The final value reached in the *X*-axis direction by FEM was 90.35 μm, whereas the final value experimentally measured was 73.88 μm, with an error of 22.3%. This higher error value must be corrected by

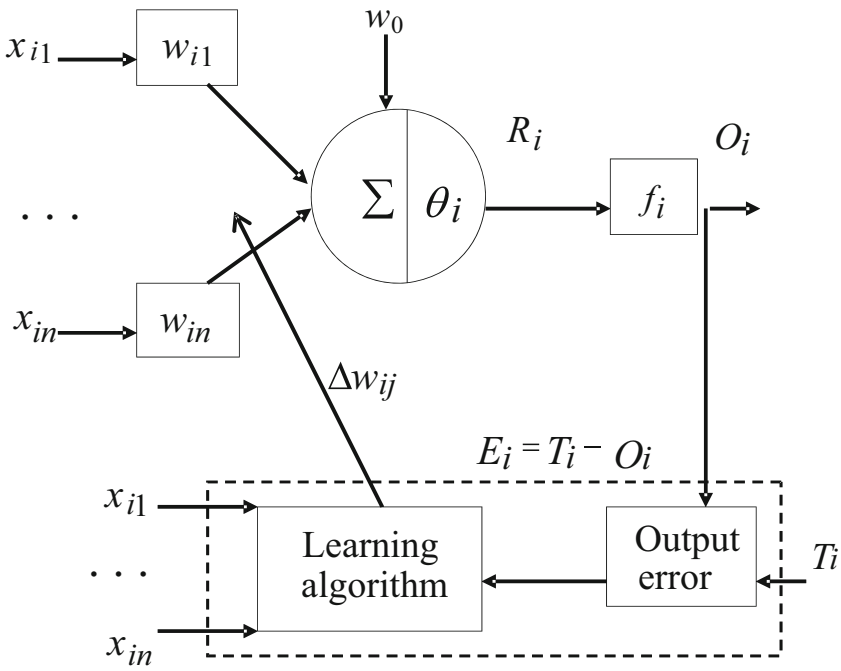

Fig. 25 Model of an artificial neuron with the supervisor (within dashed rectangle). (Adapted from [51])

Table 2 FEM temperatures during cycle #1 simulation that were not used in ANN training

Time (min)	T1 (°C)	T2 (°C)	T3 (°C)	T4 (°C)	T5 (°C)	T6 (°C)	T7 (°C)	T8 (°C)	T9 (°C)	T10 (°C)	T11 (°C)	T12 (°C)	T13 (°C)
30	26.670	23.750	22.294	21.727	21.261	21.192	22.479	21.371	21.910	22.048	21.405	21.855	21.669
60	33.080	26.628	22.875	22.069	21.550	21.664	23.205	21.739	22.402	22.710	21.808	22.449	22.169
72	34.064	27.680	23.064	22.161	21.674	21.887	23.408	21.883	22.579	22.904	21.958	22.657	22.349
90	35.288	29.082	23.381	22.273	21.864	22.229	23.652	22.092	22.825	23.245	22.169	22.914	22.604
108	36.287	30.281	23.687	22.364	22.055	22.567	23.846	22.290	23.052	23.338	22.364	23.123	22.843
120	36.855	30.979	23.878	22.418	22.185	22.785	23.953	22.417	23.193	23.448	22.498	23.243	22.995
150	38.019	32.422	24.316	22.540	22.502	23.299	24.170	22.713	23.515	23.673	22.922	23.496	23.349
180	38.911	33.523	24.706	22.653	22.808	223.761	24.335	22.981	23.798	23.852	23.308	23.706	23.673
210	39.613	34.371	25.055	22.762	23.103	24.175	24.468	23.224	24.050	23.999	23.655	23.931	23.972
228	39.966	34.787	25.249	22.827	23.274	24.402	24.538	23.358	24.191	24.077	23.846	24.058	24.140

adjusting the coefficient of heat exchange with the ambient, since in the experimental measurement, the faster thermal stabilization was clear. At the same time, the spindle tip advanced towards the machining table in the *Z*-axis direction by 19.51 μm during FEM and 17.92 μm during test cycle, with an error of 8.9%. The error in the *Y*-axis direction slightly increased, thus meaning that the spindle tip had risen in relation to the reference bushing by 14.13 μm with FEM simulation and 13.25 μm experimentally, reaching an error of 6.6%. Note that although the relative error between simulated and experimental results was above 10% at the most critical point, the tendency of the thermal error was the same in both analysis methods. A major thermal error in *Y*-axis direction could be verified during the cycle #2 result analysis, since in this case, the friction heating of the machine predominantly occurred in the *Y*-axis slide unit—ball screw and linear guide systems (see in Fig. 22).

The final value reached in the *Y*-axis direction by FEM was 73.91 μm, whereas the value experimentally obtained was 80.18 μm, with an error of 7.8%. Note that the error in the *Z*-axis direction reached 29.04 μm with FEM simulation, and 23.41 μm experimentally, with an error of 24.0%, which implied an approximation of the spindle tip to the reference bushing.

The error in the *X*-axis direction during cycle #2 increased to the opposite side of the axis in comparison to cycle #1. This implied that the machine column had a decrease in perpendicularity corresponding to the *XY* plane.

Observed in Fig. 23 are the thermal errors in cycle #5, in which the three linear slide axes—*X*/*Y*/*Z*—were moving simultaneously, the same tendency of thermal error found during cycle #1, although it presented smaller gradients, since the speed in cycle #5 was inferior to the speed used in cycles #1 and #2, except by the error in *Y*-axis direction, which in this case showed an increase as the error similar in *X*-axis direction, which is expected since both units were at the same speed and had almost the same dimensions. The final value reached in the *Y*-axis direction by FEM was 23.39 μm, whereas the value experimentally obtained was 25.23 μm with an error of 7.3%. The spindle tip advanced towards the machining table in the *Z*-axis direction by 11.36 μm during FEM and 9.84 μm during test cycle, reaching an error of 15.4%.

Performing an analysis based only on percentage errors computed between the results from the numerical simulations with the experimental results may have left the impression of a high error, as occurred in some cases by errors greater than 10%. However, the degree of complexity of the problem being modeled should be taken into account, as well as if the error tendency in the directions of the three linear axes is being achieved. In addition, the relative error calculated between the values from the two methods did not exceed 17 μm in the worst case for all cycles analyzed.

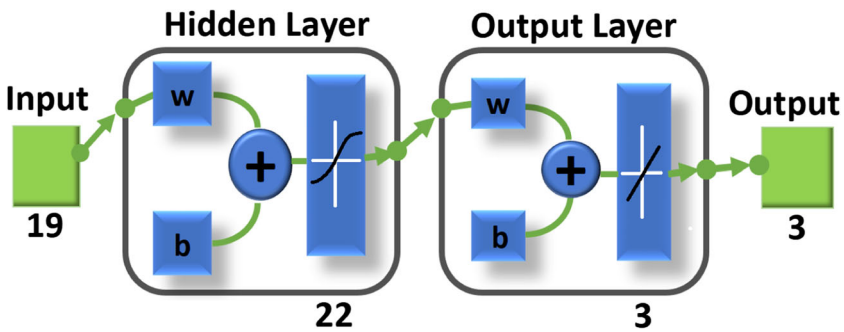

Fig. 26 Artificial neural network topology developed

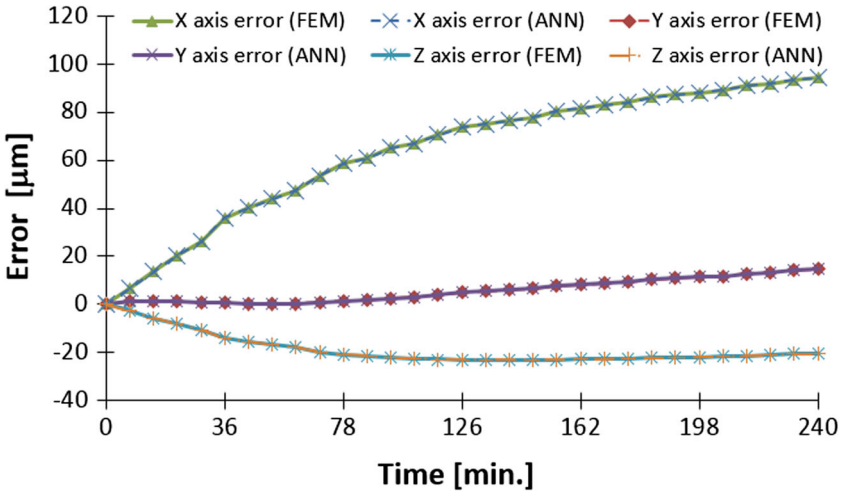

Fig. 27 Curves of the thermal errors in the *X*, *Y*, and *Z* directions obtained by FEM simulation compared with ANN learning

3.3 Analysis of numerical data through artificial neural network

The results obtained from the FEM for the temperature fields and for the thermal errors of the five cycles analyzed allowed training an artificial neural network (ANN) using MATLAB™ software to accurately predict with robustness the thermal behavior of the machining center under different operational conditions. Due to the complexity of the neural network model, a brief introduction is given below.

3.3.1 Introduction to the neural network algorithm

The neural network model is formally a network structure composed of neurons or nodes, including an input layer, hidden middle or intermediate layer, and the output layer, as shown in Fig. 24.

For the neural network model shown in Fig. 24, the input layer has three neurons, indicating that the model has three input variables, whereas the output layer has two neurons, indicating that the model has two output variables. In other words, the number of neurons in the input and output layers is determined by input variables and output variables. The hidden layer can have multiple layers, and the number of neurons in each layer may be different. The optimization of the neural network structure refers mainly to the reasonable selection of the number of hidden layers and the number of neurons in each layer [25, 51]. The principle of functioning of the neuron with supervised learning is shown in Fig. 25.

In Fig. 25, $w_{ij} = [w_{i1}, w_{i2}, \ldots, w_{in}]$ is the vector of weights of the entries of the ith neuron; $x_{ij} = [x_{i1}, x_{i2}, \ldots, x_{in}]$ is the input vector of the ith neuron; $R_i = \sum w_{ij}x_{ij}$ is the activation of

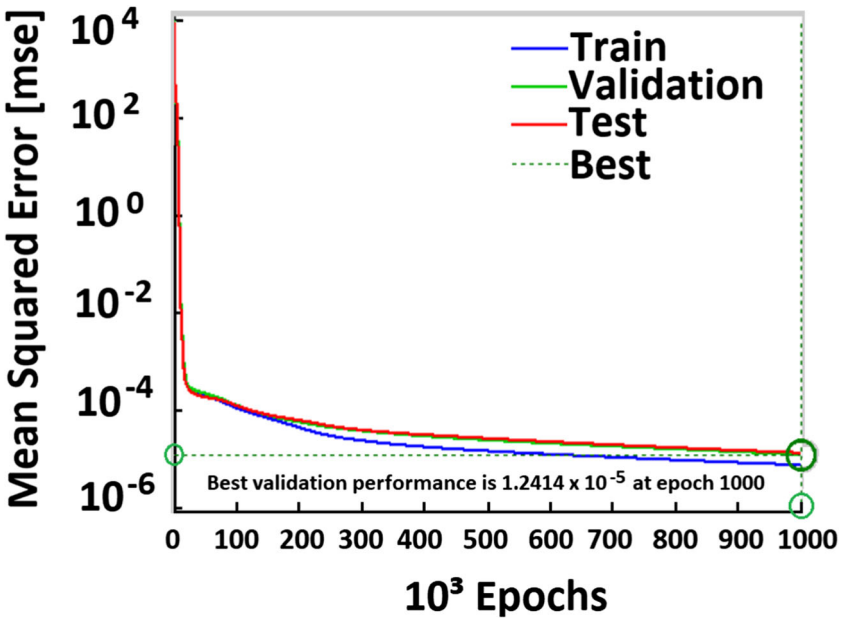

Fig. 28 ANN's learning performance chart

Table 3. FEM predicted temperatures during cycle # 4 simulation not used in ANN training

time[min]	FEM predicted temperatures [°C]												
	T1	T2	T3	T4	T5	T6	T7	T8	T9	T10	T11	T12	T13
30	28.531	23.685	22.291	27.088	22.377	21.611	31.469	22.965	26.018	24.853	22.523	21.854	23.197
60	31.519	26.544	22.877	29.900	23.277	22.415	36.761	25.230	29.261	26.987	23.929	22.394	25.409
72	32.389	27.577	23.071	30.608	23.607	22.758	38.726	26.075	30.380	27.553	24.372	22.571	26.232
90	33.482	28.955	23.337	31.409	24.069	23.264	40.140	27.238	31.869	28.202	24.928	22.812	27.402
108	34.385	30.136	23.589	31.997	24.494	23.746	41.640	28.723	33.150	28.681	25.382	23.029	28.496
120	34.906	30.824	23,772	32.309	24.758	24.051	42.488	28.894	33.902	28.933	25.640	23.165	29.185
150	35.993	32.250	24.197	32.909	25.358	24.746	44.223	30.235	35.487	29.404	26.163	23.477	30.778
180	36.853	33.340	24.851	33.352	25.883	25.350	45.574	31.321	36.736	29.728	26.561	23.757	32.207
210	37.551	34.183	24.932	33.708	26.344	25.872	46.676	32.206	37.735	29.963	26.873	24.012	33.496
228	37.911	34.597	25.129	33.894	26.594	26.150	47.253	32.659	38.241	30.076	27.045	24.154	34.210

neuron ith; $O_i = f\left(\sum_{j=1}^{n} w_{ij} \cdot x_{ij} + w_0\right)$ is the output of neuron ith; T_i is the desired output pattern; $E_i = T_i - O_i$ is the output error used during learning, and Δw_{ij} is the variation of weights during learning.

The commonly used transfer functions $f(R)$ are *sigmoid*, *tansig*, and *purelin* as follows:

$$sigmoid: \quad f(R) = \frac{1}{1 + e^{-R}} \tag{24}$$

$$tansig: f(R) = \frac{e^{R} - e^{-R}}{e^{R} + e^{-R}} \tag{25}$$

$$purelin: f(R) = R \tag{26}$$

The process of modeling with the neural network is, in fact, the process of adjusting the weights w and the limit values θ of the neurons. Naturally, if the measured values of the input variables are replaced in the neural network, the network will have output values. When the output values are compared to the measured values of output variables, the quadratic residual sum is obtained. Therefore, the modeling process is tuning the network in the direction which reduces the quadratic residual sum and replaces input variables in the new network to obtain the new quadratic residual sum for the next setting until the quadratic residual sum is small enough to be acceptable [51].

3.3.2 Development of artificial neural network

In order to optimize and minimize quadratic errors, neural networks were formulated with two layers, 22 neurons in the first layer with transfer function *tansig* and 3 neurons in the second layer, with a *purelin* transfer function. The network was *feed-forward backpropagation* with *Levenberg-Marquardt* training function (TRAINLM) and *mean squared error* (MSE) performance function. The input data were the time, the *X*/*Y*/*Z* axes speed (see in Table 1), the spindle rotation speed, and the 15 read points of temperature (see in Table 2) obtained by FEM. The output data were the thermal errors in *X*, *Y*, and *Z* axis directions reached by FEM. FEM data obtained in cycles #1, #2, #3, #4, and #5 were used to feed the ANN. The network topology is shown in Fig. 26.

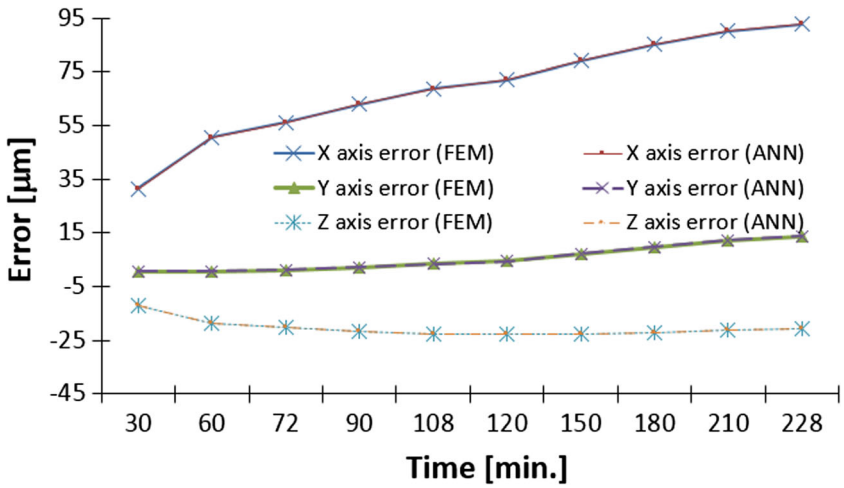

Fig. 29 Validation curves of the thermal errors in the *X*, *Y*, and *Z* axis directions obtained by FEM and ANN simulation for cycle #1

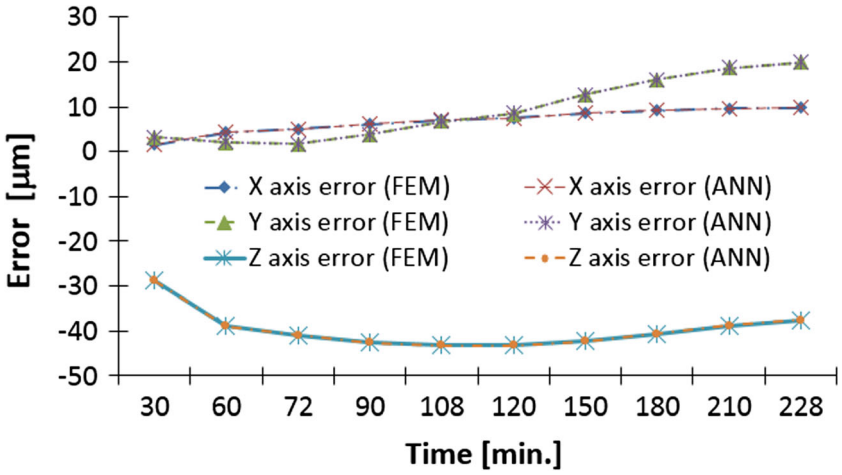

Fig. 30 Validation curves of the thermal errors in the *X*, *Y*, and *Z* axis directions obtained by FEM and ANN simulation for cycle #4

The result of the training and learning process for the three linear axes (i.e., *X*/*Y*/*Z*) using the ANN is presented in Fig. 27, which shows the learning process simultaneously for the respective thermal errors along the three axes, as a function of the temperatures developed at the critical points of the machining center analyzed in 1000 iterations. As seen in Fig. 27, convergence occurred for all axes which means that the network training was satisfactory, and the network is expected to be able to predict a result for which it has not been exposed. The temperature and thermal error data obtained during the FEM simulation of cycle #1 were used to test the network.

The performance curves for the 1000 iterations, which were extracted from the MATLAB™ environment, are shown in Fig. 28, which demonstrates that the network was able to learn and that the mean square error reached 1.2414E−5 μm compared to simulated results.

3.3.3 Validation of artificial neural network

After the network undergoes the training process, it is important to submit it to another process known as "validation." The validation process of an ANN aims to provide input data values to the network after training different from those to which it was submitted during training, in this case, different temperatures, in order to compare the thermal errors obtained by the network with the results simulated by FEM for the same temperatures and to verify if the network can effectively learn. This step aims to confirm through the developed ANN if it will be possible to predict the thermal errors by providing only the temperature values measured by the sensors or simulated by FEM.

The procedure adopted for the thermal error process of validation was the following:

- Ten time ranges and temperature ranges of the simulated result table for all the five simulated cycles were removed prior to performing the network training. For each 240-min cycle, the intervals 30′, 60′, 72′, 90′, 108′, 120′, 150′, 180′, 210′, and 228′ were removed. Thus, the ANN was trained without these temperature values. This paper shows only the temperature tables of cycles #1 (Table 2) and #4 (Table 3) due to the large amount of data collected.
- The network was fed again from the temperature data of these 10 time intervals removed for all five simulated cycles without any new training.

Table 4 Relative errors between the thermal error values in the *X*-axis direction obtained by the FEM and the thermal errors predicted by ANN for cycle #1

Time (min)	*X*-axis thermal error (FEM) (μm)	*X*-axis thermal error (FEM) (μm)	Relative error (%)
30	31.3504	31.3543	0.0124
60	50.4947	50.5226	0.0552
72	56.0431	56.0265	0.0296
90	62.9710	62.9721	0.0017
108	68.7050	68.7052	0.0003
120	72.0430	72.0403	0.0037
150	79.1650	79.1608	0.0053
180	85.0360	85.0469	0.0128
210	90.0260	90.0208	0.0058
228	92.6890	92.7018	0.0138

	Helpful to achieving the objective of the model	Harmful to achieving the objective of the model
Internal origin / attribute of the machine model organization	**STRENGTHS** • Robust methodology using both physical and experimental approaches. • Numerical simulation with subsequent experimental validation of the thermal behavior of a 5-axis machining center. • Results with good repeatability (accuracy). • Ease of implementation of the methodology in the machining center studied. • Work developed in partnership with industry.	**WEAKNESS** • Results limited to the type and model of machining center studied. • High initial expenditure of time and energy. • Need for investment in instrumentation and data acquisition and measurement equipment. • Need of acclimatized room. • Availability of at least one machining center for experimental testing.
External origin / attribute of the environment of the machine model	**OPPORTUNITIES** • Use of the methodology developed in major or minor machine tools of the same line. • Application of the methodology in machines with different design (other lines). • Implement the compensation algorithm in the machining center to perform thermal error correction in real time.	**THREATS** • High instrumentation costs to perform a robust correlation when machining a part. • Loss of model accuracy when considering tests on the factory floor.

Fig. 31 SWOT matrix evaluation of the proposed approach to control the thermal errors in a five-axis CNC machining center

The validation values were obtained after performing the process described above, i.e., the thermal errors predicted by the network, as shown in Fig. 29, for the temperatures obtained during cycle #1, and for the temperatures obtained during cycle #4, in Fig. 30. Therefore, ANN performed the error prediction inserting different temperature values from those values with which it was trained. Figure 29 graph shows the thermal error curves simulated by FEM in the *X*, *Y*, and *Z* axis directions obtained in the time intervals listed in Table 2, which correspond to the intervals not considered in ANN training.

Additionally, the curves of the thermal errors predicted by ANN for the same intervals are illustrated in Fig. 29. Thus, it is possible to conclude that the developed network could accurately predict with robustness of the thermal errors of the machining center under different working conditions from which it was trained. The same can be concluded from Fig. 30 graph, which shows the comparative results of FEM and ANN for the temperature data listed in Table 3.

The neural network developed in this research could predict the machining center thermal errors through numerically simulated temperature results, as seen in Figs. 29 and 30. The graphs, though, could not specify the relative error between the values predicted by ANN and the results from the FEM simulations. Therefore, Table 4 presents the results of thermal errors in the *X*-axis direction simulated by FEM and predicted by ANN, both from cycle #1. Also in Table 4, the percentage relative errors for the 10 time intervals not used in ANN training were calculated showing that the relative errors between FEM-simulated results and ANN-predicted results were quite low, with the maximum in the order of 0.06%. This order of magnitude for the relative error was repeated for all other validations of the network in each of the cycles.

4 SWOT matrix

An evaluation of the strengths, weakness, opportunities, and threats (SWOT) of the proposed methodology was developed. The SWOT matrix is illustrated in Fig. 31. It allows to highlight the strengths of this work, as well as to point out some improvement opportunities through future work. In Fig. 31, it is also possible to identify some weaknesses observed in relation to the developed model and threats to what has been done up to the moment.

The main strengths of this work are the partnership established with the industry and the robustness of the methodology obtained by the simultaneous physical and experimental approach. The main opportunity is associated with the implementation of the model obtained in the machine's CNC for real-time error correction. The weaknesses and threats are mainly associated with the need to consider a machining study and variable ambient temperature in the development of the thermal error compensation model of the machining center.

5 Conclusions

The general conclusion is that the methodology developed in this research that combined experimental and physical approach allowed an accurate and robust simulation of the thermomechanical behavior of the entire machining center. This work verified that the use of physical models to simulate the generation of heat by friction through the finite element method is robust and accurate when compared with the results obtained experimentally. It was possible to validate the finite element model of the entire machine for several different duty cycles. The results of the simulations showed that the methodology is an effective tool to determine and predict the thermal displacement of the machine by correlating the reading of temperatures at strategic points with the displacement at the tool tip, hence reducing the effort and analysis time to solve thermal problems in machine tools. These conclusions are justified by the practical implications listed next:

- The thermal boundary conditions based on the theory of frictional heat and heat convection applied in the FEM analysis were adequate, thus obtaining a maximum error of less than 8% when comparing the numerical results with the experimental results.
- The FEM analysis was able to simulate the thermal error behavior of the machining center in different thermal conditions represented by different duty cycles. The relative errors between the values simulated numerically with the values obtained experimentally were averaged between 6 and 15%. For cases of higher relative errors, the thermal boundary conditions should be reviewed, but even in these cases, the impact of the error is minimal since the error was always lower than 17 μm.
- After ANN validation, it was possible to conclude that the developed algorithm is an accurate and robust tool to predict the thermal errors of the machine for various working conditions, being able to predict the errors even with the machine moving at different speeds or alternating the movement of the axes. The relative error between the FEM-simulated results and the ANN-predicted results for the same time step was less than 1.0% considering all the five cycles analyzed.
- The data obtained by measuring the thermal errors in the FEM model of the machining center can also be obtained in any other model of machine tools, once the same methodology is applied.
- This methodology allows developing preliminary studies in the early design and development phase of machine tools, as well as during the trial phase, thus avoiding thermal errors affecting the machine performance.
- Thus, it can be verified that the presented methodology could be used in actual cases of real-time thermal error compensation, proceeding to a later implementation stage of the algorithm developed in this research in the CNC of the machining center.

Acknowledgements The authors would like to acknowledge the companies B. GROB do Brazil and ESSS-ANSYS for their support in providing equipment and software.

References

1. Dornfeld D, Helu MM (2008) Precision manufacturing. Springer Science + Business Media, New York ISBN 978–0–387-32467-8/ e-ISBN 978–0–387-68208-2. http://www.springer.com/gp/book/9780387324678
2. Zhu J (2008) Robust thermal error modeling and compensation for CNC machine tools. 160p. Ph.D. thesis - The University of Michigan. Ann Arbor
3. Bryan JB (1990) International status of thermal error research. Ann CIRP 39(2):645–656. https://doi.org/10.1016/S0007-8506(07)63001-7
4. Aronson RB (1990) War against thermal expansion. Manuf Eng 116(6):45–50 ISSN 0361-0853
5. Neugebauer R, Zwingenberger C, Schädlich K, Veselý K (2008) Simulation des Wärmegangs von Werkzeugmaschinen, Fraunhofer Institut für Werkzeugmaschinen und Umformtechnik, Chemnitz, Germany, IWU Forschungsvorhaben, Nr 2609, pp. 79
6. Gebhardt M (2014) Thermal behaviour and compensation of rotary axes in 5-axis machine tools, thesis doctor of sciences of ETH Zurich. Switzerland, pp. 137
7. Liu K, Li T, Wang Y, Sun M, Wu Y, Zhu T (2017) Physically based modeling method for comprehensive thermally induced errors of CNC machining centers. Int J Adv Manuf Technol 94(1-4):463–474. https://doi.org/10.1007/s00170-017-0736-9
8. Yang H, Ni J (2005) Dynamic neural network modelling for nonlinear, nonstationary machine tool thermally induced error. Int J Mach Tools Manuf 45(4–5):455–465. https://doi.org/10.1016/j.ijmachtools.2004.09.004
9. Zhang JF, Feng PF, Wu ZJ, Yu DW, Chen C (2013) Thermal structure design and analysis of a machine tool headstock. Mechanics 19(4):478–485. https://doi.org/10.5755/j01.mech.19.4.5044
10. Donmez MA, Hahn MH, Soons JA (2007) A novel cooling system to reduce thermally-induced errors of machine tools. CIRP Ann Manuf Technol 56(1):521–524. https://doi.org/10.1016/j.cirp.2007.05.124
11. Kishawy HA, Dumitrescu M, Ng EG, Elbestawi MA (2005) Effect of coolant strategy on tool performance, chip morphology and surface quality during high-speed machining of A356 aluminum alloy. Int J Mach Tools Manuf 45(2):219–227. https://doi.org/10.1016/j.ijmachtools.2004.07.003
12. Kodera T, Yokoyama K, Miyaguchi K, Nagai Y, Suzuki T, Masuda M, Yazawa T (2004) Real-time estimation of ball-screw thermal elongation based upon temperature distribution of ball-screw. JSME Int J Ser C Mech Syst Mach Elem Manuf 47(4):1175–1181. https://doi.org/10.1299/jsmec.47.1175
13. ISO 230-3 (2007) Test code for machine tools–part 3: determination of thermal effects. Geneva
14. ISO 10791-10, (2007), Test conditions for machining centers–part 10: evaluation of thermal distortion. Geneva
15. ISO 13041-8 (2004) Test conditions for numerically controlled turning machines and turning centers–part 8: evaluation of thermal distortions. Geneva
16. Mayr J, Jedrzejewski J, Uhlmann E, Donmez MA, Knapp W, Härtig F, Wendt K, Moriwaki T, Shore P, Schmitt R, Brecher C, Wu T, Wegener K (2012) Thermal issues in machine tools. CIRP

Ann Manuf Technol 61(2):771–791. https://doi.org/10.1016/j.cirp.2012.05.008
17. ISO 230-1 (2012) Test code for machine tools–part 1: geometric accuracy of machines operating under no-load or quasi-static conditions. Geneva
18. Yang S, Yuan J, Ni J (1996) Accuracy enhancement of a horizontal machining center by real-time error compensation. J Manuf Syst 15(2):113–124. https://doi.org/10.1016/0278-6125(96)82336-3
19. Miao EM, Gong YY, Niu PC, Ji CZ, Chen HD (2013) Robustness of thermal error compensation modeling models of CNC machine tools. Int J Adv Manuf Technol 69(9):2593–2603. https://doi.org/10.1007/s00170-013-5229-x
20. Yang JG (1998) Error synthetic compensation technique and application for NC machine tools, Doctor Thesis, Shanghai Jiaotong University, Shanghai
21. Miao E, Liu Y, Liu H, Gao Z, Li W (2015) Study on the effects of changes in temperature-sensitive points on thermal error compensation model for CNC machine tool. Int J Mach Tool Manu 97:50–59. https://doi.org/10.1016/j.ijmachtools.2015.07.004
22. Attia MH, Fraser S (1999) A generalized modeling methodology for optimized real-time compensation of thermal deformation of machine tools and CMM structures. Int J Mach Tools Manuf 39(6):1001–1016. https://doi.org/10.1016/S0890-6955(98)00063-7
23. Xu M, Jiang S, Cai Y (2007) An improved thermal model for machine tool bearings. Int J Mach Tools Manuf 47(1):53–62. https://doi.org/10.1016/j.ijmachtools.2006.02.018
24. Creighton E, Honegger A, Tulsian A, Mukhopadhyay D (2010) Analysis of thermal errors in a high-speed micro-milling spindle. Int J Mach Tools Manuf 50(4):386–393. https://doi.org/10.1016/j.ijmachtools.2009.11.002
25. Liu H, Miao EM, Wei XY, Zhuang XD (2017) Robust modeling method for thermal error of CNC machine tools based on ridge regression algorithm. Int J Mach Tool Manu 113:35–48. https://doi.org/10.1016/j.ijmachtools.2016.11.001
26. Vanherck P, Dehaes J, Nuttin M (1997) Compensation of thermal deformation in machine tools with neural nets. Comput Ind 33(1):119–125. https://doi.org/10.1016/S0166-3615(97)00016-X
27. Yang QD, Van den Bergh C, Vanherck P, Kruth J (1999) Linear regression and neural net models applied to thermal error compensation in machine tools. Eur J Mech Environ Eng 44(3):146–152 ISSN: 00353612, 13716980
28. Mize CD, Ziegert JC (2000) Neural network thermal error compensation of a machining center. Precis Eng 24(4):338–346. https://doi.org/10.1016/S0141-6359(00)00044-1
29. Zhang Y, Yang J, Jiang H (2012) Machine tool thermal error modeling and prediction by gray neural network. Int J Adv Manuf Technol 59(9–12):1065–1072. https://doi.org/10.1007/s00170-011-3564-3
30. Shi H, Ma C, Yang J, Zhao L, Mei X, Gong G (2015) Investigation into effect of thermal expansion on thermally induced error of ball screw feed drive system of precision machine tools. Int J Mach Tools Manuf 97(10):60–71. https://doi.org/10.1016/j.ijmachtools.2015.07.003
31. Liu K, Sun M, Zhu T, Wu Y, Liu Y (2016) Modeling and compensation for spindle's radial thermal drift error on a vertical machining center. Int J Mach Tools Manuf 105(6):58–67. https://doi.org/10.1016/j.ijmachtools.2016.03.006
32. Uhlmann E, Hu J (2012) Thermal modelling of a high speed motor spindle. Proc. 5th CIRP - Conference on High Performance Cutting 2012. Procedia CIRP 1(2012):313–318. doi:https://doi.org/10.1016/j.procir.2012.04.056
33. Lee SK, Yoo JH, Yang MS (2003) Effect of thermal deformation on machine tool slide guide motion. Tribol Int 36(1):41–47. https://doi.org/10.1016/S0301-679X(02)00128-7
34. Li X, Xu J (2016) Analysis of fluid-solid-thermal coupling for ball screw in boring-milling machining center. Shenyang University, China. Proc. 13th Global Congress Manufacturing & Management, GCMM 2016. Zhengzhou-China, Nov 28th–30th. 2016. MATEC Web of Conferences, v.100 (2017), n. 2., Ed. Zhao et al., EDP Science, France/USA, ISBN 9781510837485 http://www.proceedings.com/33837.html
35. Li F, Li T, Wang H, Jiang Y (2017) A temperature sensor clustering method for thermal error modeling of heavy milling machine tools. MDPI. Appl Sci 7(1):82. https://doi.org/10.3390/app7010082
36. Chen TC, Chang CJ, Hung JP, Lee RM, Wang CC (2016) Real-time compensation for thermal errors of the milling machine. MDPI. Appl Sci 6(4):101. https://doi.org/10.3390/app6040101
37. Harris TA (2001) Rolling bearing analysis, 4th edn. Wiley, New York ISBN 0-471-35457-0
38. Takabi J, Khonsari MM (2013) Experimental testing and thermal analysis of ball bearings. Tribol Int 60:93–103. https://doi.org/10.1016/j.triboint.2012.10.009
39. Harris TA, Barnsby RM (1998) Tribological performance prediction of aircraft gas turbine main shaft ball bearings. Tribol Trans 41(1):60–68. https://doi.org/10.1080/10402009808983722
40. Palmgren A, Ruley B (1945) Ball and roller bearing engineering. SKF Industries Inc.; SKF Industries Inc., Philadelphia
41. Tu JF, Stein JL (1998) Model error compensation for observer design. Int J Control 69(2):329–345. https://doi.org/10.1080/002071798222875
42. Xu ZZ, Liu XJ, Kim HK, Shin JH, Lyu SK (2011) Thermal error forecast and performance evaluation for an air-cooling ball screw system. Int J Mach Tool Manu 51(7–8):605–611. https://doi.org/10.1016/j.ijmachtools.2011.04.001
43. Verl A, Frey S (2010) Correlation between feed velocity and preloading in ball screw drives. CIRP Ann Manuf Technol 59(1):429–432. https://doi.org/10.1016/j.cirp.2010.03.136
44. Cheng DJ, Park JH, Suh JS, Kim SJ, Park CH (2017) Effect of frictional heat generation on the temperature distribution in roller linear motion rail surface. J Mech Sci Technol 31(3):1477–1487. https://doi.org/10.1007/s12206-017-0247-5
45. Jang SH, Kim GH, Park CH (2017) Estimation of friction heat in a linear motion bearing using Box-Behnken design. Int J Adv Manuf Technol 89(5–8):2021–2029. https://doi.org/10.1007/s12206-017-0247-5
46. Cheng DJ, Yang WS, Park H, Park TJ, Kim SJ, Kim GH, Park CH (2014) Friction experiment of linear motion roller guide THK SRG25. Int J Precis Eng Manuf 15(3):545–551. https://doi.org/10.1007/s12541-014-0369-y
47. Gleich S (2008) Simulation des thermischen Verhaltens spanender Werkzeug maschinen in der Entwurfsphase. 107 p., Dr.-Ing. Thesis, Fakultät für Maschinenbau der Technischen-Universität Chemnitz, Germany
48. Li X, Xu J (2017) Analysis of fluid-solid-thermal coupling for ball screw in boring-milling machining center. Procedia Eng 174:530–536. https://doi.org/10.1016/j.proeng.2017.01.182
49. Li H, Shin Y (2004) Integrated dynamic thermo-mechanical modeling of high speed spindles, part I: model development. Trans ASME J Manuf Sci Eng 126(1):148–158. https://doi.org/10.1115/1.1644545
50. Haitao Z, Yang J, Shen J (2007) Simulation of thermal behavior of a CNC machine tool spindle. Int J Mach Tool Manu 47(6):1003–1010. https://doi.org/10.1016/j.ijmachtools.2006.06.018
51. Haykin S (1998) Neural network: a comprehensive foundation, 2nd edn. Pearson Prentice Hall, Singapore 823 pp., ISBN 978-0132733502